Competitive binding-mediated mesoscale protein-protein interactions direct microtubule growth

Zhiyi Wei (weizy@sustech.edu.cn)
Southern University of Science and Technology https://orcid.org/0000-0002-4446-6502

Xuanyan Jia
Southern University of Science and Technology

Leishu Lin
Southern University of Science and Technology https://orcid.org/0000-0002-1214-4760

Siqi Guo
Southern University of Science and Technology

Lulu Zhou
Southern University of Science and Technology

Gaowei Jin
Southern University of Science and Technology

Jiayuan Dong
Southern University of Science and Technology

Jinman Xiao
Southern University of Science and Technology

Xingqiao Xie
Southern University of Science and Technology

Yiming Li
Southern University of Science and Technology

Sicong He
Southern University of Science and Technology

Cong Yu
Southern University of Science and Technology https://orcid.org/0000-0003-2912-6347

Biological Sciences - Article

Keywords:

Posted Date: February 1st, 2024

DOI: https://doi.org/10.21203/rs.3.rs-3681467/v1

Additional Declarations: There is **NO** Competing Interest.

Competitive binding-mediated mesoscale protein-protein interactions direct microtubule growth

Xuanyan Jia[1,2,6,7], Leishu Lin[1,2,7], Siqi Guo[2], Lulu Zhou[3], Gaowei Jin[1,2], Jiayuan Dong[1,2], Jinman Xiao[1,2], Xingqiao Xie[1,2,4], Yiming Li[3], Sicong He[2], Cong Yu[2,5,*], Zhiyi Wei[1,2,4,*]

[1]Brain Research Center, Southern University of Science and Technology, Shenzhen, Guangdong 518055, China.

[2]School of Life Sciences, Southern University of Science and Technology, Shenzhen, Guangdong 518055, China.

[3]Department of Biomedical Engineering, Southern University of Science and Technology, Shenzhen, Guangdong 518055, China.

[4]Shenzhen Key Laboratory of Biomolecular Assembling and Regulation, Shenzhen, Guangdong 518055, China.

[5]Guangdong Provincial Key Laboratory of Cell Microenvironment and Disease Research, and Shenzhen Key Laboratory of Cell Microenvironment, Shenzhen, Guangdong 518055, China.

[6]SUSTech-HIT Joint PhD Program, Harbin Institute of Technology, Harbin, Heilongjiang 150001, China.

[7]These authors contributed equally.

[*]Correspondence: Z.W. (weizy@sustech.edu.cn) and C.Y. (yuc@sustech.edu.cn)

Abstract

Microtubule organization in cells relies on targeting mechanisms [1–4]. CLASP proteins are key regulators of microtubule organization [5,6], yet the underlying mechanisms remain elusive. Here, we revealed that the C-terminal domain of CLASP2 interacts with a common motif found in several CLASP2-binding proteins. This interaction drives the dynamic localization of CLASP2 to distinct cellular compartments, where CLASP2 accumulates in protein condensates at the cell cortex or the microtubule plus end. These condensates physically contact with each other via CLASP2-mediated competitive binding, determining cortical microtubule targeting. The phosphorylation of CLASP2 modulates the dynamics of the condensate-condensate interaction and spatiotemporally navigates microtubule growth. Moreover, we identified additional CLASP-interacting proteins that are involved in condensate contacts in a CLASP2-dependent manner, uncovering a general mechanism governing microtubule targeting. Our findings not only unveil a tunable multiphase system regulating microtubule organization, but also offers general mechanistic insights into intricate protein-protein interactions at the mesoscale level.

Main

Microtubules (MTs) grow in a highly organized pattern, with oscillation between growth and shrinkage at their plus ends, allowing rapid reconfiguration in response to cellular cues [1–4,7]. The dynamic growth of MTs requires the accumulation of specialized proteins at the MT plus end, known as plus end tracking proteins (+TIPs) [5,8]. As crucial +TIPs, cytoplasmic linker proteins (CLIPs), CLIP-associated proteins (CLASPs), and ending-binding proteins (EBs), act as molecular liaisons, orchestrating interactions between MTs and various cellular compartments, including the cell cortex [6]. However, given the intricate interactions among MTs, +TIPs, and compartmentalized protein assemblies, the molecular mechanisms governing the spatial organization of MTs in different cellular regions remain largely elusive.

CLASPs play an essential role in MT organization within various cellular compartments [9–11]. The *CLASP* gene has been found in a wide range of organisms, from yeast and plants to mammals [12–14]. Mammalian CLASPs contain two paralogs, CLASP1 and CLASP2, each consisting of three tumor-overexpressed-gene (TOG) domains for MT binding, a C-terminal CLIP-interacting domain, and two Ser-X-Ile-Pro (SxIP) motifs binding to EBs (Fig. 1a) [15]. The binding of CLASPs to different proteins regulates the localization of CLASPs in various cellular compartments. For instance, CLIP170, a member of the CLIP family, guides CLASPs to the MT plus end and regulates their activity in preventing MT catastrophe [9,14]. GCC185, a Golgi coiled-coil protein, recruits CLASPs to the Golgi apparatus and promotes Golgi-directed microtubule growth [16,17]. Centromere-associated protein E (CENP-E), a kinesin motor, associates with CLASPs, facilitating the targeting of MTs to the kinetochore during cell division [18]. Additionally, CLASPs and membrane-associated scaffold protein LL5β are involved in the formation of the cortical MT stabilization complex (CMSC), anchoring MTs to focal adhesions (FAs) at the cell cortex and regulate FA dynamics [19,20]. Despite the crucial role of the CLASP-mediated interactions in targeting MTs to the diverse cellular compartments, the underlying molecular mechanisms remain elusive.

Identification of a consensus sequence for CLASP2 binding

To elucidate the molecular basis of the CLASP-mediated interaction, we mapped the regions critical for binding to the TOG4 domain of CLASP2 in both CLIP170 and LL5β, using analytical size exclusion chromatography (aSEC) and isothermal titration calorimetry (ITC)-based measurements. The binding region in CLIP170 was narrowed down to a N-terminal coiled coil (CLIP170_CC) (Extended Data Fig. 1a-c), while the minimal TOG4-binding motif in LL5β (LL5β_TBM) was identified to contain only 19 residues within a predicted coiled coil (LL5β_CC) (Extended Data Fig. 1d-f). With the mapped interacting regions, we determined the TOG4 structures of CLASP2 in complex with the identified fragments of CLIP170 and LL5β, respectively, by using crystallography (Extended Data Table 1).

In these crystal structures, the TOG4 domain adopts a typical α-solenoid fold, comprising 11 α-helices (Fig. 1b), closely resembling the structures of other TOG domains in CLASP2 (Fig. 1c). Our local structural alignments further delineated the TOG domains in CLASP2 into two lobes, the N-lobe and the C-lobe (Extended Data Fig. 2a and 2b). CLIP170_CC forms a dimeric coiled coil,

interacting with the C-lobes from two TOG4 fragments (Fig. 1d). Notably, a short, yet highly conserved sequence in CLIP170_CC is involved in TOG4 binding (Extended Data Fig. 2c and 2d). This interaction is characterized by the insertion of F443 in CLIP170_CC into a pocket formed by the last two α-helices in the C-lobe (Fig. 1e). In addition, several negatively charged residues (e.g., E446) in CLIP170_CC form salt bridges with positively charged residues at the groove (Fig. 1e).

Similar to CLIP170, LL5β employs an α-helix to interact with the CLIP170-binding groove in CLASP2_TOG4 (Fig. 1f and 1g). The similar TOG4-binding mode of CLIP170 and LL5β indicates the TOG4 domain may be used for recognizing other CLASP-binding proteins. Remarkably, a similar sequence pattern, termed TOG4-binding motif or TBM, was also found in the conserved coiled-coil regions of CENP-E and GCC185 (Extended Data Fig. 2c and 2d). ITC-based analyses confirmed the interactions between CLASP2_TOG4 and potential TBM-containing fragments of CENP-E and GCC185 (Fig. 1j and Extended Data Fig. 3). By solving the CLASP2_TOG4 structure in complex with the CENP-E fragment (Fig. 1h and 1i), we validated the binding of CENP-E TBM to the TOG4 domain.

Crucially, all four identified TBMs exhibit a common sequence feature with two strictly conserved residues, a phenylalanine (F) and a glutamic acid (E), in the middle of their sequences (Fig. 1k). In our complex structures, these two residues adopt essentially identical conformations to tightly pack with the TOG4 domain (Fig. 1e, 1g, and 1i). The critical role of these two residues in the TOG4/TBM interaction were strongly supported by our ITC data (Fig. 1j and Extended Data Fig. 3), showing the profound disruption on the TOG4/TBM interaction by mutating these two positions. Taken together, the above biochemical, structural, and sequence analyses demonstrate that despite having distinct overall sequence, the four CLASP-binding proteins share a characteristic TBM sequence essential for their specific interaction with CLASPs via the TOG4 domain (Fig. 1l).

The TOG4/TBM interaction is essential for CLASP2 targeting in cells

The TBM-binding groove in the TOG4 domain is highly conserved in CLASPs across different plant and animal species (Extended Data Fig. 2b and 4a), suggesting a fundamental role for the TOG4/TBM interaction in the function of CLASP family members. Our structural analysis revealed that two critical residues, $L1467^{CLASP2}$ and $R1435^{CLASP2}$, located at the center of the TBM-binding groove (Extended Data Fig. 4a), directly interact with the two key residues, F and E, in the TBMs, respectively (Fig. 1e, 1g, 1i, and Extended Data Fig. 4b). Consistent with the structural finding, two disruptive mutations, L1467E and R1435E, within the groove blocked the binding of the TOG4 domain to the four TBMs (Extended Data Fig. 4c).

To analyze the role of the TOG4/TBM interaction in the cellular distribution of CLASP2, we overexpressed CLASP2α, the longest isoform of CLASP2, and its variants in HeLa cells. As reported previously [14,19–22], CLASP2α accumulated at the MT plus end (Extended Data Fig. 4d) and depolymerizing MTs via nocodazole treatment promoted CLASP2α targeting to the vicinity of FAs (Extended Data Fig. 4e). However, either the TOG4 deletion mutant or the TBM-binding deficient mutations (L1467E and R1435E) resulted in a diminished enrichment of CLASP2α in these cellular

locations (Extended Data Fig. 4d-g). Considering the crucial role of CLIP170 and LL5β in recruiting CLASP2 to the MT plus end and the FA vicinity, respectively [14,19], these observations indicate the requirement of the specific TOG4/TBM interaction in the cellular localization of CLASP2.

Given that these TBM-containing proteins share the same binding site in the TOG4 domain, these proteins likely compete for the binding to CLASPs. Indeed, our aSEC analyses showed that CLIP170 can outcompete other TBM-containing proteins for binding to CLASP2_TOG4 in solution (Extended Data Fig. 5). Given the TOG4-mediated enrichment of CLASP2α in the MT plus end and several specific cellular compartments, this binding competition likely occurs between CLIP170 and the compartmentalized TBM-containing proteins in the place where the MT plus end is anchored, such as the plus end-tethered CMSCs in the vicinity of FAs [19,23,24]. It raises an intriguing question regarding how CLASP proteins orchestrate MT dynamics and organization in different cellular compartments amid such competing interactions.

ELKS co-phase separates with LL5β in the recruitment of CLASP2 to the FA vicinity

To explore the mechanism governing the FA vicinity localization of CLASP2 and MTs, we focused on two key components of the CMSC, LL5β and ELKS, which associate with each other and play important roles in regulating the cortical localization of CLASPs and MTs [19,25] (Fig. 2a). The ELKS protein family in mammals contains two closely related members, ELKS1 and ELKS2 [26]. We identified the minimal regions in both LL5β (ELKS-binding motif or EBM) and ELKS2 (CC3), which are essential and sufficient for mediating the ELKS/LL5β interaction (Extended Data Fig. 6a-c). As the EBM sequence does not overlap with the TBM in LL5β, LL5β may simultaneously bind to CLASPs and ELKSs. Indeed, a LL5β fragment containing both binding motifs (LL5β_2BM) formed a tripartite complex with CLASP2_TOG4 and the CC3 fragment of ELKS2 (Extended Data Fig. 6d).

By determining the crystal structure of the ELKS2_CC3/LL5β_EBM complex (Extended Data Table 1), we found that the dimeric ELKS2_CC3 interacts with two LL5β_EBM fragments, each consisting of an α-helical hairpin (Fig. 2b). The extensive interactions observed in the structure contribute to the stable association of LL5β with ELKSs (Extended Data Fig. 6e). Among these interactions, $R290^{ELKS2}$ (corresponding to R294 in ELKS1) plays a critical role by forming several salt bridges and hydrogen bonds with LL5β_EBM (Fig. 2c). Charge-reverse mutations (R290E in ELKS2 and R294E in ELKS1) abolished the binding of LL5β to the ELKS proteins in solution (Extended Data Fig. 6f and 6g). Consistently, LL5β lost its colocalization with $ELKS1^{R294E}$ puncta in HeLa cells (Fig. 2d).

In line with the previous finding that ELKS1 promotes the clustering of CLASP2 at the cell cortex [19], the overexpression of ELKS1 significantly enhanced the accumulation of CLASP2α around FAs in nocodazole-treated cells (Fig. 2e). However, the $ELKS1^{R294E}$ mutant failed to enrich CLASP2α in the vicinity of FAs (Fig. 2e and 2f), indicating that the cortical accumulation of CLASP2 depends on the formation of the LL5β/ELKS1 complex. Interestingly, the removal of the N-terminal intrinsic disorder region (IDR) from ELKS1 resulted in the diffused distribution of ELKS1 and a reduction

in the accumulation of CLASP2α around FAs (Fig. 2e and 2f). It is noteworthy that ELKS proteins undergo IDR-dependent liquid-liquid phase separation (LLPS) and form co-condensates with interacting proteins [27–30]. Hence, we speculated that ELKS1 may accumulate LL5β and CLASP2 via LLPS.

Indeed, the purified full-length protein of ELKS1 co-phase separated with LL5β_2BM in solution (Fig. 2g). Conversely, LL5β_2BM promotes ELKS1 LLPS by reducing the concentration threshold to 0.5 μM (Extended Data Fig. 7a), a level comparable with the cellular concentration of ELKS proteins [31]. In contrast, the E439K mutation in LL5β and the L1467E mutation in CLASP2, which disrupt the LL5β/ELKS (Fig. 2c) and CLASP2/LL5β (Fig. 1g) interactions, respectively, blocked the accumulation of LL5β_2BM and CLASP2_TOG4 in the ELKS1 condensate (Fig. 2g and 2h). In line with the observed condensate formation in solution, both endogenous and transfected ELKS1 in HeLa cells formed small condensates in an IDR-dependent manner (Extended Data Fig. 7b). ELKS1, but not its R294E mutant, is capable of accumulating CLASP2α in cellular condensates (Extended Data Fig. 7c and 7d). These results collectively suggest that LL5β accumulates in the ELKS1 condensate by binding to ELKS1 and consequently recruits CLASP2 into condensates.

To verify this scenario in cells, we designed a chimeric protein by replacing the IDR of ELKS1 with the N-terminal domain of Par3 (P3N), which have a distinct sequence from ELKS1_IDR and is known to form cellular condensates through LLPS [32]. Interestingly, the ΔIDR/+P3N chimaera regained the ability to form condensates that can specifically recruit LL5β (Extended Data Fig. 7b and 7e). Importantly, this chimeric protein also restored the accumulation of CLASP2α in the FA vicinity (Fig. 2e and 2f). Thus, the LLPS propensity of ELKS1 may drive condensate formation beneath the plasma membrane, in coordinating with LL5β, which can bind to the phospholipid through its PH domain [19] and recruits CLASP2 via the TOG4/TBM interaction (Fig. 2i).

CLASP2 accumulation in ELKS1 and CLIP170 condensates is required for cortical MT targeting

Given the critical role of CLASPs in stabilizing MTs, ELKS1 may regulate cortical MT organization by recruiting CLASP proteins. To explore this possibility, we analyzed the distribution of MTs in nocodazole-treated cells overexpressing ELKS1 or its variants. After nocodazole washout, MTs in cells overexpressing wild-type ELKS1 massively reached the cell edge, in stark contrast to the perinuclear distribution of MTs in control cells (Fig. 2j and 2k). Consistent with the impaired ability to accumulate CLASP2, neither the LL5β binding-deficient mutant (R294E) nor LLPS-deficient mutant (ΔIDR) of ELKS1 promoted MT growth towards the cell edge, whereas the ΔIDR/+P3N chimaera showed a promotion on cortical MT growth like wild-type ELKS1 (Fig. 2j and 2k). Given that CLASP2 is assembled with ELKS1 and LL5β to form CMSCs around FAs [23] (Fig. 2a and Extended Data Fig. 8a), we speculated that the ELKS1 condensate facilitates MT attachment to FAs. Supporting this hypothesis, the ELKS1 condensates in the FA vicinity closely contact with the MT plus end (Fig. 2l). Together, these results suggest that the ELKS1 condensate plays a crucial role in targeting MTs to the cell cortex through creating a CLASP2-enriched environment that stabilizes the attached MT plus end.

In addition to its enrichment in the ELKS1 condensate, CLASP2 also accumulates at the MT plus end in a TOG4-dependent manner (Fig. 2a and Extended Data Fig. 4d). Disrupting the TOG4/TBM interaction eliminated the enrichment of CLASP2 in the CLIP170 puncta at the MT plus end (Extended Data Fig. 8b). Interestingly, CLIP170 also forms condensates wrapping around the MT ends in HeLa cells [33] (Extended Data Fig. 8c) and undergoes phase separation [34] (Extended Data Fig. 8d), which are capable of accumulating CLASP2 through the TOG4/TBM interaction (Fig. 2m). Intriguingly, the CLIP170 condensate at the MT plus end closely contact with the cortical ELKS1 condensate (Extended Data Fig. 8e), suggesting a role of the CLIP170 condensate in targeting MTs to the cell cortex. Consistently, deleting the C-terminal zinc finger (ZnF) domain from CLIP170 disrupt its ability for condensate formation (Extended Data Fig. 8d) and cortical MT organization (Extended Data Fig. 8f and 8g).

However, given the competition between the TBMs of CLIP170 and LL5β for binding to CLASP2 (Extended Data Fig. 5a), it remains puzzling how the MT plus-end enriched with CLIP170 can tether to the ELKS1 condensate enriched with LL5β and how CLASP2-mediated interactions function in this tethering (Fig. 2n).

Competitive binding to accumulated CLASP2 mediates the stable contact between condensates

To explore these questions, we analyzed the LLPS of ELKS1 and CLIP170 in cells co-transfected with these proteins. The two proteins formed droplets separately in the cytosol, occasionally touching each other in an immiscible manner (Fig. 3a1 and Extended Data Movie 1). Strikingly, upon the additional overexpression of LL5β and CLASP2α in this multiphase system, the ELKS1 droplet became trapped onto the surface of the CLIP170 droplet (Fig. 3a2 and Extended Data Movie 1), with the average contact duration extended from ~2 minutes to more than 12 minutes (Fig. 3b). Remarkably, in about half measurements, the two types of droplets remained in contact throughout the 20-minute observation (Fig. 3b), indicating that the presence of CLASP2 dramatically prolongs droplet adhesion. Interestingly, this stable contact could still occur in the absence of LL5β overexpression (Fig. 3a3, 3b, and Extended Data Movie 1), presumably due to the presence of endogenous LL5β in the ELKS1 condensate (Fig. 2d). This unexpected finding suggests a role of the interaction between the ELSK1 and CLIP170 condensates in the regulation of MT tethering to the vicinity of FAs.

In agreement with the CLASP2-dependent condensate interaction, in cells transfected with LL5β but not CLASP2α, the prolonged contact duration was diminished (Fig. 3a4, 3b, and Extended Data Movie 1). Similarly, either depleting CLASP2α from the droplets by introducing the TBM-binding deficient mutation (L1467E) in CLASP2α or removing LL5β from the ELKS1 droplet by introducing the LL5β-binding deficient mutation (R294E) in ELKS1 abolished the prolonged droplet adhesion (Fig. 3a5, 3a6, 3b, and Extended Data Movie 1). Consistent with our live imaging analysis, the 3D reconstruction of cytosolic droplets further confirmed the requirement of CLASP2α

in the droplet attachment (Extended Data Fig. 9a). These results demonstrate that CLASP2 is essential for the stable attachment between the ELKS1 and CLIP170 condensates.

Since LL5β and CLIP170 compete for binding to CLASP2, we asked whether competitive binding contributes to the CLASP2-mediated condensate interaction. Thus, we designed the CLASP2α^{+PDZ} chimaera by fusing the PDZ domain of RIM1 to the C-terminus of CLASP2α (Fig. 3c). As the RIM1 PDZ domain can interact with the PDZ binding motif (PBM) at the C-terminus of ELKS1 [35], CLASP2α^{+PDZ} acquires the ability to directly bind to ELKS1 (Extended Data Fig. 9b). Upon overexpressing CLASP2α^{+PDZ} and ELKS1^{R294E}, competitive binding was replaced with uncompetitive binding in the new multiphase system (Fig. 3d1). Interestingly, CLIP170 and ELKS1 co-phase separated in this new system (Fig. 3d1), likely because the binding of CLASP2α^{+PDZ} to CLIP170 and ELKS1^{R294E} are compatible, allowing mixed distribution of CLIP170 and ELKS1 in the condensed phase. As a control, deleting the PBM from ELKS1^{R294E} blocked the accumulation of CLASP2α^{+PDZ} in the ELKS1 condensate (Extended Data Fig. 9b), resulting in separated condensates of CLIP170 and ELKS1 (Fig. 3d2). Although competitive binding occurs, the wild-type ELKS1 protein also co-condensed with CLIP170 in the presence of CLASP2α^{+PDZ} (Fig. 3d3), indicating that the uncompetitive binding of CLASP2α^{+PDZ} to ELKS1 surpasses the competitive binding for the co-condensate formation. As expected, ELKS1$^{\Delta PBM}$ that lacks uncompetitive binding while remains competitive binding to CLASP2α^{+PDZ}, reestablished the condensate attachment (Fig. 3d4 and Extended Data Fig. 9b). Therefore, we concluded that the condensate attachment relies on the competitive binding of LL5β and CLIP170 to CLASP2, which likely mediates mesoscale protein-protein interactions between the attached droplets (Extended Data Fig. 9c).

As shown by live imaging analysis, many CLASP2α clusters intermittently moved towards the growing leading edge (Extended Data Movie 2). This dynamic accumulation of CLASP2α results in the predominant distribution of CLASP2α clusters near the cell edge (Extended Data Fig. 9d-f). These observations suggest that CLASP2 may delocalize from the ELKS1 condensate and move with the CLIP170 condensate at the MT plus end. However, cellular localization analysis of CLASP2α^{+PDZ} showed a different pattern. It forms co-puncta with ELKS1 and CLIP170 (Extended Data Fig. 9d), and more than half of CLASP2α^{+PDZ} puncta were located away from the cell edge (Extended Data Fig. 9e). It is likely that the co-condensate formation prevents the detachment of the CLIP170 condensate from the ELKS1 condensate, thereby inhibiting the redistribution of CLASP2α from the co-condensate. Thus, the competitive rather than uncompetitive binding allows the condensate attachment and detachment, regulating the dynamic distribution of CLASP2 in cortical MT organization.

Intriguingly, although LL5β and CLIP170 having comparable binding affinities to CLASP2 (Fig. 1j), the accumulation level of CLASP2α in the ELKS1 droplet is significantly lower than that in the CLIP170 droplet (Fig. 3e). This difference may be attributed to the indirect recruitment of CLASP2α to the ELKS1 condensate. Surprisingly, the accumulation ratio of CLASP2α in the two condensates spatiotemporally determines the condensate interaction mode. With increasing CLASP2α levels in the ELKS1 droplet, the CLIP170 droplet tended to engulf the ELKS1 droplet,

covering a larger surface area (Fig. 3e and 3f). Moreover, quantitative analysis revealed that elevating CLASP2α levels in the ELKS1 droplet to more than 25% of that in the CLIP170 droplet efficiently extends the droplet contact duration (Fig. 3g and Extended Data Fig. 9g), presumably due to the larger contact area between droplets. Thus, the strength of the condensate attachment is regulated by the accumulation level of CLASP2 in the two condensates, indicating a control mechanism for condensate interaction via the modulation of CLASP2 levels in these condensates.

Phosphorylation of CLASP2 controls the detachment of the MT plus end from the ELKS1 condensate for the directional growth of MTs

The cellular distribution of the ELKS1 condensate is not restricted to the cell periphery. Many ELKS1 condensates were found to be formed away from both FAs and the cell edge (Extended Data Fig. 10a and 10b). While a large portion of the ELKS1 condensates disappeared as the leading edge of the cell expanded, some ELKS1 condensates persist and thereby can be observed away from the cell edge (highlighted by white circles in Extended Data Movie 2). Intriguingly, the path of MTs often overlapped with several ELKS1 condensates in a row (Fig. 4a). Superresolution microscopic analysis confirmed the spatial proximity of MTs to the ELKS1 condensates (Extended Data Fig. 10c). Importantly, through monitoring the growing MT plus end, indicated by CLIP170 signals, we found that cortical MTs passed through multiple ELKS1 condensates behind the leading edge and showed transient contacts with these condensates (Fig. 4b and Extended Data Movie 3). It suggests that the ELKS1 condensates distal to the cell edge may play a role in navigating MT growth towards the cell edge.

To verify the role of ELKS1 in directing cortical MT organization, we prepared cells with ELKS1 knockdown (Extended Data Fig. 11a). To quantitatively assess the organization of cortical MTs, two-dimensional Fourier transform was applied to the pattern of MT distribution at the cell periphery (Fig. 4c). Unlike the typical radial organization of MTs at the cell periphery with an anisotropic distribution, depletion of ELKS1 led to disorganized cortical MTs with a tendency towards isotropic distribution (Extended Data Fig. 11b and 11c). Resembling the effect of ELKS1 knockdown, disorganized cortical MTs was also observed in cells with LL5β knockdown (Extended Data Fig. 11a-c), further supporting the function of ELKS1 and LL5β in accumulating CLASP2 and organizing MT growth at the cell cortex. Consistently, knocking down both CLASP1 and CLASP2 resulted in impaired cortical MT organization [22] (Fig. 4d, 4e and Extended Data Fig. 11d). Together, these results indicate that the ELKS1 condensates contribute to directional MT growth by orchestrating the CMSC components, including LL5β and CLASP2.

When the MT plus end attaches to an ELKS1 condensate, how does it detach rapidly from the condensate to continue the MT growth? As a high level of CLASP2 is required for the stable contact between the CLIP170 and ELKS1 condensates (Fig. 3e), the detachment may be achieved by lowering the CLASP2 level in the ELKS1 condensate. CLASPs have been reported to be phosphorylated by GSK3β [24,36], and overexpression of either GSK3β or a phosphomimetic mutant of CLASP2 (8S/D), which replaces eight serine phosphorylation sites with aspartic acids, led to directionless MT growth (Fig. 4f) [24]. Thus, it is tempting to speculate that the phosphorylation of

CLASP2 by GSK3β may inhibit its accumulation in the ELKS1 condensate, considering the importance of electrostatic interactions in regulating protein recruitment to condensates [37,38].

In line with this hypothesis, the accumulation level of the CLASP2α 8S/D mutant in the ELKS1 condensate was significantly decreased in either low or high expression levels (Fig. 4g, 4h, and Extended Data Fig. 12a and 12b). Furthermore, the direct addition of eight aspartic acids (+8D) to the C-terminus of CLASP2α attenuated its accumulation in the ELKS1 condensate (Fig. 4g, 4h, and Extended Data Fig. 12a and 12b), confirming the charge-mediated prevention of CLASP2 entry into the condensed phase of ELKS1. Remarkably, CLASP2$^{8S/D}$ still accumulated in the CLIP170 condensate in the cytosol or MT ends, with the level comparable to that of the wild-type protein (Extended Data Fig. 12c-e). This indicates that the phosphorylation-dependent inhibition of CLASP2 accumulation in the condensed phase is selective. Consistent with the decreased CLASP2α level of the 8S/D and +8D mutants in the ELKS1 condensate, the droplet attachment between the ELKS1 and CLIP170 condensates became significantly less stable (Fig. 4i and 4j). Thus, GSK3β-phosphorylation of CLASP2 likely modulates the condensate attachment. Importantly, similar to the observation that CLASP2α^{L1467E}, the TBM-binding deficient mutant, failed to restore the cortical MT organization in CLASP1/2 double knockdown cells, CLASP2α$^{8S/D}$ was also unable to rescue the phenotype (Fig. 4d and 4e), indicating that the regular arrangement of cortical MTs requires tunable CLASP2 levels in the ELKS1 condensates.

Consistent with the previous observation that the GSK3β activity is inhibited in the cell edge [24,39], the ELKS1 condensates in the cell periphery accumulate more CLASP2 than those in the cell interior (Extended Data Fig. 12f). Therefore, in the region distal to the cell edge, the GSK3β-dependent phosphorylation of CLASP2 to enable dynamic contact between the ELKS1 and CLIP170 condensates for MT navigation by specifically decreasing CLASP2 levels in the ELKS1 condensate (Fig. 4k). On the other hand, in the FA vicinity proximal to the cell edge, high CLASP2 levels in the ELKS1 condensate may promote stable contact between the two condensates for MT anchoring (Fig. 4k).

The CLASP-mediated condensate attachment is a general paradigm for TBM-containing proteins

As MTs are recruited to various cytoplasmic compartments, it is appealing to explore additional proteins involved in the cellular targeting of CLASPs via the TOG4-mediated interaction. To identify potential TBM-containing proteins in the human genome, we employed the consensus sequence pattern for TBMs (Fig. 1k), taking into account additional criteria such as intracellular localization and the helical conformation of TBMs. After careful selection, we identified seven candidate proteins (Fig. 5a), most of which have been reported to associate with MTs [40–44].

Among these proteins, we focused on Janus kinase and MT interacting protein 1 (JAKMIP1) and CENP-J were selected for further validation, as previous studies had suggested them as being part of complexes with CLASPs [18,45]. Co-immunoprecipitation assay demonstrated that CLASP2, but not its L1467E mutant, binds to both JAKMIP1 and CENP-J (Fig. 5b and 5c). Notably, the addition

of CENP-E_CC in the assay reduced the binding of CLASP2 to JAKMIP1 and CENP-J (Fig. 5b and 5c). Furthermore, ITC-based analyses confirmed that the TBM fragments of JAKMIP1 and CENP-J interact with CLASP2_TOG4 (Fig. 5d and 5e). Thus, we concluded that both JAKMIP1 and CENP-J directly bind to CLASP2 through the specific TOG4/TBM interaction. Our findings are consistent with a recent study that also identified CENP-J as a potential binding partner for the TOG4 domain in CLASP1 [46].

Interestingly, both JAKMIP1 and CENP-J form protein condensates in transfected cells (Extended Data Fig. 13a), suggesting the potential for CLASP2-mediated mesoscale association between the CLIP170 condensate and these condensates. Indeed, by co-expressing either JAKMIP1 or CENP-J with CLIP170 and CLASP2α in cells, we observed the stable attachment of the CLIP170 condensate to the JAKMIP1 and CENP-J condensates in a CLASP2-dependent manner, relying on the TOG4-mediated interaction (Fig. 5f-i). Given that these TBM-containing proteins form cellular condensates (Extended Data Fig. 13a), it is likely that such condensate attachments mediated by CLASP2_TOG4 represent a common feature for TBM-containing proteins to regulate MT organization in various cellular compartments. Notably, the 8S/D mutation of CLASP2 had minimal impact on the adhesive contact between these condensates (Extended Data Fig. 13b-d), as $CLASP^{8S/D}$ remained highly enriched in the JAKMIP1 and CENP-J condensates (Extended Data Fig. 13e-h). This finding indicates that the JAKMIP1 and CENP-J condensates are insensitive to phosphorylated CLASP2, and GSK3β may not be a critical regulator of the mesoscale association between CLIP170 and JAKMIP1 or CENP-J via CLAPS2.

Remarkably, our sequence analysis of the CLASP family proteins across a spectrum of organisms, ranging from yeast to human, showed that the TBM-binding site in the TOG4 domain is conserved in plants and animals (Extended Data Fig. 14). In addition to the TOG4 domain, the SxIP motifs have been found to promote the localization of CLASPs at the MT plus-end by binding to EBs and facilitate cortical MT organization [22,24,47] (Fig. 1a). However, the SxIP motifs appear in vertebrates but absent in most invertebrates. This observation suggests a fundamental role for the TOG4/TBM interaction in organizing MTs (Fig. 5j), which remains to be explored in different cellular compartments and different organisms (e.g., dynamic MT network in growth cone [48,49] and cortical MT organization in plants [50,51]).

Discussion

By employing an integrative approach involving structural, biochemical, and cellular techniques, our study here revealed a multiphase system governing the regular organization of MTs at the cell cortex. This intricate system relies on CLASP2, which serves as a molecular glue, mediating the interactions between the CLIP170 and ELKS1 condensates through two different modes: the transient interaction navigating MT growth towards the cell edge and the stable association anchoring MTs to FAs (Fig. 4k). Given the highly dynamic nature of MT growth, the protein assemblies in this system demands rapid regulation, which is efficiently achieved through LLPS. Importantly, our findings highlight the significance of competitive binding in drives protein-

protein interaction at the mesoscale level, offering a plausible mechanism to dynamically manage the intricate interplay of different protein condensates in cells.

Biomolecular condensates have been widely characterized in diverse cellular processes [52–54]. Emerging evidence has suggested the co-existence of multiple condensates in certain cellular milieu [55–58], yet the condensate organization in a multiphase system has remained largely a mystery. Our study unveiled the dynamic interaction between immiscible condensates in the multiphase system mediated by competitive binding. In the dilute phase, proteins are excluded from binding sites by competing molecules and then quickly diffuse away. However, in the condensed phase, the concentrated environment limits protein diffusion [59], allowing previously disassociated molecules to reassociate. Crucially, unlike the single TBM-binding site in a CLASP2 molecule, the condensed CLASP2 assembly can provide multiple TBM-binding sites for interacting with different TBM-containing proteins simultaneously (Extended Data Fig. 9c). Consequently, rather than exclusive interactions in the dilute phase, competitive binding likely mediates condensate-condensate interaction through mesoscale protein-protein interactions at the contact interface between condensates. On the other hand, competitive binding prevents the mixing of two closely attached condensates, as competing molecules in these two condensates are mutually excluded. The substitution of competitive binding with uncompetitive binding leads to co-condensate formation (Fig. 3d), which mixes all interacting proteins and thereby limits the dynamic distribution of proteins. Thus, competitive binding is favorable for the reversible association and dissociation of the MT plus end with the ELKS1 condensate. Considering the prevalence of binding competitions, our discovery provides a potential organization mode for multiphase systems in cellular processes, which require dynamic associations between immiscible condensates. Interestingly, in addition to CLIP170, EB1 was reported to undergo LLPS as well [60], suggesting a multiphase organization at the MT plus end. As EB1 has similar affinities for binding to the SxIP motifs of CLASPs and CLIP170 [61], it raises the intriguing possibility that the SxIP-mediated competitive binding of CLASPs and CLIP170 to EB1 play a role in organizing these protein condensates at the MT plus ends.

An important feature of the CLASP2-mediated condensate interaction is its tunability, which allows for precise control of directional MT growth (Fig. 4k). This tunability is achieved through the GSK3β-mediated phosphorylation of CLASP2. When MTs are growing towards the leading edge, active GSK3β phosphorylates CLASP2 and consequently reduces the CLASP2 level in the ELKS1 condensate, which shortens the duration of the condensate contact and allows MTs to continue growing. Notably, GSK3β can substantially inhibits the accumulation of CLASP2 at the MT plus-end, partly by the disrupted binding of phospho-CLASP2 to EBs [14,21,24,36], which may also contribute to the shortened contact duration. Once MTs reach the leading edge, decreased GSK3β activity promotes the accumulation of CLASP2 in the ELKS1 condensate, leading to a stable anchoring of the MT plus-ends to cortical FAs. The dynamic concentration changes in the condensed phase indicates the role of CLASP2 as a “client” in the multiphase system. The “client” role of CLASP2 allows cells to regulate the CLASP2 level rapidly and selectively in the condensates without affecting condensate formation. As CLASPs are recruited to various cellular compartments by different TBM-containing proteins, the CLASP-mediated condensate interaction likely plays a role

in MT organization in cellular compartments other than the cell cortex, such as the Golgi apparatus (Fig. 5j), regarding the LLPS propensity of GCC185 [62].

While FAs are critical players in MT guidance [63,64], the underlying mechanisms have remained poorly understood. CMSC proteins are known to regulate the interplay between MTs and FAs. As the core component of the CMSC, ELKS1 forms condensates with LL5β, generating a widespread network at the cell cortex (Fig. 2d and Extended Data Fig. 7b). These condensates act as hotspots that dynamically associate with the MT plus end for MT guidance. During cell migration, with the leading edge advances, while most ELKS1 condensates disassembled, a subset persists (Extended Data Movie 2). As these residual ELKS1 condensates marks the former edge, they likely serve as guidance cues, directing MTs to grow in alignment with the migrating leading edge. In addition, ELKS proteins are known to participate in vesicle docking and release at both the cell cortex and presynaptic terminals [19,65]. Given the proximity of the ELKS1 condensate to MTs and the plasma membrane, these condensates may also serve as effective platforms for capturing and releasing vesicles transported by kinesin motors [27]. Nevertheless, as the ELKS1 condensate are tethered to the plasma membrane through the association of LL5β with phospholipids [19], the effect of ELKS1 on MT organization is likely confined to MTs close to the plasma membrane. MTs located away from the plasma membrane, particularly those in the cell interior, may be organized by other mechanisms. One such alternative mechanism involves actin filaments, which have been indicated in guiding MT growth through actin-MT crosstalk [66]. How the different mechanisms coordinate MT growth requires further investigations to provide a comprehensive understanding of MT organization in cells.

References

1. Akhmanova, A. & Kapitein, L. C. Mechanisms of microtubule organization in differentiated animal cells. *Nature Reviews Molecular Cell Biology* vol. 23 541–558 (2022).
2. Gudimchuk, N. B. & McIntosh, J. R. Regulation of microtubule dynamics, mechanics and function through the growing tip. *Nature Reviews Molecular Cell Biology* vol. 22 777–795 (2021).
3. Conde, C. & Cáceres, A. Microtubule assembly, organization and dynamics in axons and dendrites. *Nature Reviews Neuroscience* vol. 10 319–332 (2009).
4. Muroyama, A. & Lechler, T. Microtubule organization, dynamics and functions in differentiated cells. *Development (Cambridge)* vol. 144 3012–3021 (2017).
5. Akhmanova, A. & Steinmetz, M. O. Microtubule +TIPs at a glance. *J. Cell Sci.* **123**, 3415–3419 (2010).
6. Akhmanova, A. & Noordstra, I. Linking cortical microtubule attachment and exocytosis. *F1000Research* **6**, (2017).
7. Howard, J. & Hyman, A. A. Growth, fluctuation and switching at microtubule plus ends. *Nature Reviews Molecular Cell Biology* vol. 10 569–574 (2009).
8. Akhmanova, A. & Steinmetz, M. O. Control of microtubule organization and dynamics: Two ends in the limelight. *Nature Reviews Molecular Cell Biology* vol. 16 711–726 (2015).
9. Aher, A. *et al.* CLASP Suppresses Microtubule Catastrophes through a Single TOG Domain. *Dev. Cell* **46**, 40-58.e8 (2018).
10. Lawrence, E. J. *et al.* Human CLASP2 specifically regulates microtubule catastrophe and rescue. *Mol. Biol. Cell* **29**, 1168–1177 (2018).
11. Aher, A. *et al.* CLASP Mediates Microtubule Repair by Restricting Lattice Damage and Regulating Tubulin Incorporation. *Curr. Biol.* **30**, 2175-2183.e6 (2020).
12. Ambrose, J. C., Shoji, T., Kotzer, A. M., Pighin, J. A. & Wasteneys, G. O. The Arabidopsis CLASP gene encodes a microtubule-associated protein involved in cell expansion and division. *Plant Cell* **19**, 2763–2775 (2007).
13. Bratman, S. V. & Chang, F. Stabilization of Overlapping Microtubules by Fission Yeast CLASP. *Dev. Cell* **13**, 812–827 (2007).
14. Akhmanova, A. *et al.* CLASPs Are CLIP-115 and -170 Associating Proteins Involved in the Regional Regulation of Microtubule Dynamics in Motile Fibroblasts. *Cell* **104**, 923–935 (2001).
15. Lawrence, E. J., Zanic, M. & Rice, L. M. CLASPs at a glance. *J. Cell Sci.* **133**, (2020).
16. Efimov, A. *et al.* Asymmetric CLASP-dependent nucleation of noncentrosomal microtubules at the trans-Golgi network. *Dev. Cell* **12**, 917–30 (2007).
17. Miller, P. M. *et al.* Golgi-derived CLASP-dependent microtubules control Golgi organization and polarized trafficking in motile cells. *Nat. Cell Biol.* **11**, 1069–1080 (2009).
18. Maffini, S. *et al.* Motor-Independent Targeting of CLASPs to Kinetochores by CENP-E Promotes Microtubule Turnover and Poleward Flux. *Curr. Biol.* **19**, 1566–1572 (2009).
19. Lansbergen, G. *et al.* CLASPs Attach Microtubule Plus Ends to the Cell Cortex through a Complex with LL5β. *Dev. Cell* **11**, 21–32 (2006).
20. Stehbens, S. J. *et al.* CLASPs link focal-adhesion-associated microtubule capture to localized

exocytosis and adhesion site turnover. *Nat. Cell Biol.* **16**, 561–73 (2014).
21. Wittmann, T. & Waterman-Storer, C. M. Spatial regulation of CLASP affinity for microtubules by Rac1 and GSK3β in migrating epithelial cells. *J. Cell Biol.* **169**, 929–939 (2005).
22. Mimori-Kiyosue, Y. *et al.* CLASP1 and CLASP2 bind to EB1 and regulate microtubule plus-end dynamics at the cell cortex. *J. Cell Biol.* **168**, 141–53 (2005).
23. Bouchet, B. P. *et al.* Talin-KANK1 interaction controls the recruitment of cortical microtubule stabilizing complexes to focal adhesions. *Elife* **5**, (2016).
24. Kumar, P. *et al.* GSK3β phosphorylation modulates CLASP-microtubule association and lamella microtubule attachment. *J. Cell Biol.* **184**, 895–908 (2009).
25. Ribolla, L. M. *et al.* Interfering with the ERC1-LL5β interaction disrupts plasma membrane-Associated platforms and affects tumor cell motility. *PLoS One* **18**, e0287670 (2023).
26. Held, R. G. & Kaeser, P. S. ELKS active zone proteins as multitasking scaffolds for secretion. *Open Biol.* (2018) doi:10.1098/rsob.170258.
27. Jin, G. *et al.* Structural basis of ELKS/Rab6B interaction and its role in vesicle capturing enhanced by liquid-liquid phase separation. *J. Biol. Chem.* **299**, 104808 (2023).
28. Liang, M. *et al.* Oligomerized liprin-α promotes phase separation of ELKS for compartmentalization of presynaptic active zone proteins. *Cell Rep.* **34**, 108901 (2021).
29. Sala, K. *et al.* The ERC1 scaffold protein implicated in cell motility drives the assembly of a liquid phase. *Sci. Rep.* **9**, 13530 (2019).
30. McDonald, N. A., Fetter, R. D. & Shen, K. Assembly of synaptic active zones requires phase separation of scaffold molecules. *Nature* **588**, 454–458 (2020).
31. Cho, N. H. *et al.* OpenCell: Endogenous tagging for the cartography of human cellular organization. *Science (80-.).* **375**, (2022).
32. Liu, Z. *et al.* Par complex cluster formation mediated by phase separation. *Nat. Commun.* **11**, (2020).
33. Jijumon, A. S. *et al.* Lysate-based pipeline to characterize microtubule-associated proteins uncovers unique microtubule behaviours. *Nat. Cell Biol.* **24**, 253–267 (2022).
34. Miesch, J., Wimbish, R. T., Velluz, M. C. & Aumeier, C. Phase separation of +TIP networks regulates microtubule dynamics. *Proc. Natl. Acad. Sci. U. S. A.* **120**, (2023).
35. Lu, J., Li, H., Wang, Y., Südhof, T. C. & Rizo, J. Solution structure of the RIM1α PDZ domain in complex with an ELKS1b C-terminal peptide. *J. Mol. Biol.* **352**, 455–466 (2005).
36. Watanabe, T. *et al.* Phosphorylation of CLASP2 by GSK-3β regulates its interaction with IQGAP1, EB1 and microtubules. *J. Cell Sci.* **122**, 2969–2979 (2009).
37. Kamagata, K. *et al.* Molecular principles of recruitment and dynamics of guest proteins in liquid droplets. *Sci. Rep.* **11**, (2021).
38. Jo, Y., Jang, J., Song, D., Park, H. & Jung, Y. Determinants for intrinsically disordered protein recruitment into phase-separated protein condensates. *Chem. Sci.* **13**, (2022).
39. Etienne-Manneville, S. & Hall, A. Cdc42 regulates GSK-3β and adenomatous polyposis coli to control cell polarity. *Nature* **421**, 753–756 (2003).
40. Yu, N. *et al.* Isolation of Functional Tubulin Dimers and of Tubulin-Associated Proteins from Mammalian Cells. *Curr. Biol.* **26**, 1728–1736 (2016).
41. Steindler, C. *et al.* Jamip1 (Marlin-1) defines a family of proteins interacting with Janus

kinases and microtubules. *J. Biol. Chem.* **279**, 43168–43177 (2004).
42. Mack, G. J. & Compton, D. A. Analysis of mitotic microtubule-associated proteins using mass spectrometry identifies astrin, a spindle-associated protein. *Proc. Natl. Acad. Sci. U. S. A.* **98**, 14434–14439 (2001).
43. Vandenbrouck, Y., Pineau, C. & Lane, L. The Functionally Unannotated Proteome of Human Male Tissues: A Shared Resource to Uncover New Protein Functions Associated with Reproductive Biology. *J. Proteome Res.* **19**, 4782–4794 (2020).
44. Coutton, C. *et al.* Mutations in CFAP43 and CFAP44 cause male infertility and flagellum defects in Trypanosoma and human. *Nat. Commun.* **9**, (2018).
45. Berg, J. M. *et al.* JAKMIP1, a Novel Regulator of Neuronal Translation, Modulates Synaptic Function and Autistic-like Behaviors in Mouse. *Neuron* **88**, 1173–1191 (2015).
46. Gareil, N. *et al.* An unconventional TOG domain is required for CLASP localization. *Curr. Biol.* **33**, 3522–3528 (2023).
47. Patel, K., Nogales, E. & Heald, R. Multiple domains of human CLASP contribute to microtubule dynamics and organization in vitro and in Xenopus egg extracts. *Cytoskeleton* **69**, 155–165 (2012).
48. Hur, E.-M. *et al.* GSK3 controls axon growth via CLASP-mediated regulation of growth cone microtubules. *Genes Dev.* **25**, 1968–1981 (2011).
49. Lee, H. *et al.* The microtubule plus end tracking protein orbit/MAST/CLASP acts downstream of the tyrosine kinase Abl in mediating axon guidance. *Neuron* **42**, 913–926 (2004).
50. Thoms, D., Vineyard, L., Elliott, A. & Shaw, S. L. CLASP facilitates transitions between cortical microtubule array patterns. *Plant Physiol.* **178**, 1551–1567 (2018).
51. Ambrose, C., Allard, J. F., Cytrynbaum, E. N. & Wasteneys, G. O. A CLASP-modulated cell edge barrier mechanism drives cell-wide cortical microtubule organization in Arabidopsis. *Nat. Commun.* **2**, (2011).
52. Banani, S. F., Lee, H. O., Hyman, A. A. & Rosen, M. K. Biomolecular condensates: Organizers of cellular biochemistry. *Nature Reviews Molecular Cell Biology* vol. 18 285–298 (2017).
53. Zhang, H. *et al.* Liquid-liquid phase separation in biology: mechanisms, physiological functions and human diseases. *Science China Life Sciences* vol. 63 953–985 (2020).
54. Chen, X., Wu, X., Wu, H. & Zhang, M. Phase separation at the synapse. *Nat. Neurosci.* **23**, 301–310 (2020).
55. Lafontaine, D. L. J., Riback, J. A., Bascetin, R. & Brangwynne, C. P. The nucleolus as a multiphase liquid condensate. *Nature Reviews Molecular Cell Biology* vol. 22 165–182 (2021).
56. Sanders, D. W. *et al.* Competing Protein-RNA Interaction Networks Control Multiphase Intracellular Organization. *Cell* **181**, 306-324.e28 (2020).
57. Courchaine, E. M. *et al.* DMA-tudor interaction modules control the specificity of in vivo condensates. *Cell* **184**, 3612-3625.e17 (2021).
58. Wu, X. *et al.* Vesicle Tethering on the Surface of Phase-Separated Active Zone Condensates. *Mol. Cell* **81**, 13-24.e7 (2021).
59. Shen, Z. *et al.* Biological condensates form percolated networks with molecular motion properties distinctly different from dilute solutions. *Elife* **12**, (2023).

60. Song, X. *et al.* Phase separation of EB1 guides microtubule plus-end dynamics. *Nat. Cell Biol.* **25**, 79–91 (2023).
61. Chen, Y., Wang, P. & Slep, K. C. Mapping multivalency in the CLIP-170 –EB1 microtubule plus-end complex. *J. Biol. Chem.* **294**, 918–931 (2019).
62. Ziltener, P., Rebane, A. A., Graham, M., Ernst, A. M. & Rothman, J. E. The golgin family exhibits a propensity to form condensates in living cells. *FEBS Lett.* **594**, 3086–3094 (2020).
63. Huda, S. *et al.* Microtubule guidance tested through controlled cell geometry. *J. Cell Sci.* **125**, 5790–5799 (2012).
64. Seetharaman, S. & Etienne-Manneville, S. Microtubules at focal adhesions - a double-edged sword. *Journal of cell science* vol. 132 (2019).
65. Nyitrai, H., Wang, S. S. H. & Kaeser, P. S. ELKS1 Captures Rab6-Marked Vesicular Cargo in Presynaptic Nerve Terminals. *Cell Rep.* **31**, 107712 (2020).
66. Dogterom, M. & Koenderink, G. H. Actin–microtubule crosstalk in cell biology. *Nat. Rev. Mol. Cell Biol.* **20**, 38–54 (2019).
67. Otwinowski, Z. & Minor, W. Processing of X-ray Diffraction Data Collected in Oscillation Mode . *Methods Enzymol.* **276**, 307–326 (1997).
68. Terwilliger, T. C. *et al.* Decision-making in structure solution using Bayesian estimates of map quality: the PHENIX AutoSol wizard. *Acta Crystallogr D Biol Crystallogr* **65**, 582–601 (2009).
69. Storoni, L. C., McCoy, A. J. & Read, R. J. Likelihood-enhanced fast rotation functions. *Acta Crystallogr D Biol Crystallogr* **60**, 432–438 (2004).
70. Sammito, M. *et al.* ARCIMBOLDO-LITE: Single-workstation implementation and use. *Acta Crystallogr. Sect. D Biol. Crystallogr.* **71**, 1921–1930 (2015).
71. Collaborative Computational Project, N. 4. The CCP4 suite: programs for protein crystallography. *Acta Crystallogr D Biol Crystallogr* **50**, 760–763 (1994).
72. Adams, P. D. *et al.* PHENIX: A comprehensive Python-based system for macromolecular structure solution. *Acta Crystallogr. Sect. D Biol. Crystallogr.* **66**, 213–221 (2010).
73. Emsley, P. & Cowtan, K. Coot: model-building tools for molecular graphics. *Acta Crystallogr D Biol Crystallogr* **60**, 2126–2132 (2004).
74. Sala, K., Raimondi, A., Tonoli, D., Tacchetti, C. & de Curtis, I. Identification of a membrane-less compartment regulating invadosome function and motility. *Sci. Rep.* **8**, 1164 (2018).
75. Hotta, A. *et al.* Laminin-based cell adhesion anchors microtubule plus ends to the epithelial cell basal cortex through LL5α/β. *J. Cell Biol.* **189**, 901–917 (2010).
76. Li, Y. *et al.* Global fitting for high-accuracy multi-channel single-molecule localization. *Nat. Commun.* **13**, (2022).

Acknowledgements

We thank the assistance of Southern University of Science and Technology (SUSTech) Core Research Facilities and Shanghai Synchrotron Radiation Facility (beamlines 17U1, 18U1, and 19U1). We are grateful to Dr. Fengfeng Niu for his valuable suggestions in improving our manuscript. This work was supported by the National Natural Science Foundation of China (Grant No. 31971131 to Z.W., 32170697 and 32370743 to C.Y., 32371009 to X.X., 32101211 to S.H., and 62375116 to Y.L.), Shenzhen Science and Technology Program (RCJC20210609104333007), Shenzhen-Hong Kong Institute of Brain Science, Shenzhen Fundamental Research Institutions (2023SHIBS0002), Shenzhen Science and Technology Innovation Commission (Grant No. JCYJ20220818100416036 and KQTD20200820113012029), and Key Technology Research and Development Program of Shandong (2021CXGC010212).

Author contributions: C.Y. and Z.W. conceived and supervised the project. X.J., L.L., S.G., L.Z., G.J., J.D., J.X., X.X. designed and performed experiments. X.J., L.L., Y.L., S.H., C.Y., and Z.W. analyzed the data. X.J., L.L., C.Y., and Z.W. wrote the manuscript with inputs from other authors.

Competing interests: The authors declare that they have no competing interests.

Data and materials availability: The structure factors and atomic models of CLASP2_TOG4 in complex with CLIP170, LL5β, and CENP-E and the LL5β/ELKS2 complex have been deposited in the Protein Data Bank (PDB) with accession code 8WHH, 8WHI, 8WHJ, 8WHK, 8WHL, and 8WHM.

Materials and Methods

Plasmids

For cellular assays, the genes of human CLASP2 (GeneBank, NM_001365634.1), rat ELKS1 (NM_170788.2), rat ELKS2 (NM_001401498.1), human CLIP170 (NM_001247997.2), human LL5β (NM_001134439.2), human GCC185 (NM_181453.3), human CENP-J (NM_018451.4) and human JAKMIP1 (NM_001099433.1) were amplified from human or rat cDNA library and then cloned into a pEGFP-C1, pmCherry-C1, or modified pcDNA3.1 vector with an N-terminal 3×Flag tag. The chimeric proteins, ELKS1$^{\Delta IDR/+P3N}$ and CLASP2α^{+PDZ}, were designed by replacing the IDR (residues 1 – 137) of ELKS1 with the N-terminal domain (residues 2 – 82) of Par3 (NM_031235.1) and by fusing the PDZ domain (residues 575 – 684) of RIM1 (XM_017596673) to the C-terminus of CLASP2α, respectively. Human CENP-E (NM_001286734.2) fragments were synthetized by Tsingke Biological Technology. For protein production, ELKS1 and CLIP170 were cloned into a pCAG vector with an N-terminal Flag tag. CLASP2_TOG4 (residues 1251 – 1479) and fragments of ELKS1, ELKS2, LL5β, CLIP170, GCC185, CENP-E, JAKMIP1, and CENP-J were subcloned into a modified pET-32a vector with an N-terminal thioredoxin (Trx)-His_6-tag. Mutagenesis was performed using the Mut Express II Fast Mutagenesis Kit V2 (Vazyme Biotech). All plasmids were extracted using the MiniPrep or MaxiPrep Kit (TransGen Biotech) and were subsequently sequenced for verification.

Antibodies

The primary antibodies used in this study included mouse anti-β-tubulin (Sangon Biotech, D1930693), 1:500 dilution for immunofluorescence (IF), rabbit anti-Paxillin (Abcam, ab32115), 1:200 dilution for IF, rabbit anti-TGN46 (Proteintech, 13573-1-AP), 1:500 dilution for IF, rabbit anti-CLASP1 (Abcam, ab108620), 1:3000 dilution for western blot (WB), rat anti-CLASP2 (Absea, 32006E03), 1:1000 dilution for WB, rabbit anti-ELKS1 (Proteintech, 22211-1-AP), 1:500 dilution for IF and 1:1000 dilution for WB, rabbit anti-LL5β (Proteintech, 22211-1-AP), 1:500 dilution for IF and 1:1000 dilution for WB, mouse anti-GAPDH (Transgene, HC301-02), 1:3000 dilution for WB, mouse anti-GFP (Transgene, HT801), 1:3000 dilution for WB, and mouse anti-Flag (Sigma, F1804), 1:3000 dilution for WB. The secondary antibodies used in this study included anti-mouse IgG HRP-linked antibody (Cell Signaling Technology, 7076S), anti-rabbit IgG HRP-linked antibody (Cell Signaling Technology, 7074S), and anti-rat IgG HRP-linked antibody (Cell Signaling Technology, 7077S), 1:3000 dilution for WB, and Alexa Fluor 488/594/647–conjugated anti-mouse/rabbit IgG antibody (Invitrogen), 1:3000 dilution for IF.

Protein expression and purification

The protein fragments were expressed in BL21(DE3) *E. coli* and induced with 0.2 mM IPTG in LB medium at 16 °C. Following induction, cells were harvested, resuspended in a binding buffer containing 50 mM Tris pH 7.5, 500 mM NaCl, 5 mM imidazole, and 1 mM phenylmethylsulfonyl fluoride, and lysed using an ultrahigh-pressure homogenizer (ATS, AH-BASICI). The lysate was centrifuged at 20,000 rpm for 30 min. The supernatant was directly applied to a Ni-NTA agarose column that had been pre-equilibrated with the binding buffer. The target protein was eluted with a buffer containing 50 mM Tris pH 7.5, 500 mM NaCl, and 300 mM imidazole and further purified

using a size-exclusion column (HighLoad 26/60 Superdex-200, GE Healthcare) with a buffer containing 50 mM Tris pH 7.5, 100 mM NaCl, 1 mM EDTA, and 1 mM dithiothreitol (DTT). The Se-Met derivative CLASP2-TOG4 was produced in M9 minimal medium supplemented with 100 mg/L of lysine, phenylalanine, and threonine, and 50 mg/L of isoleucine, leucine, valine, and selenomethionine (Se-Met). The purification of Se-Met derivative protein was the same as described above.

The full-length proteins of ELKS1, CLIP170, and their mutants were expressed in HEK 293F cells. After 3-day expression, the HEK cells were collected and rinsed with the PBS buffer. The cells were then lysed using ultrasonication in an ice-bath with a lysis buffer containing 50 mM Tris pH 7.5, 300 mM NaCl, 2 mM $MgCl_2$, 0.5% Triton X-100, 1 mM DTT, 1 mM EGTA, and protease inhibitor cocktail (TargetMol). The cell lysate was centrifuged at 20,000 rpm for 30 min, and the resulting supernatant was then loaded onto anti-Flag beads (GenScript) followed by a 1-hour incubation. After extensive washing, the target protein was eluted with the lysis buffer without Triton X-100, supplemented with Flag peptide (500 μg/ml). The eluted protein was further purified using a size exclusion column (Superdex increase-6, GE Healthcare) with a buffer containing 50 mM Tris pH 7.5, 300 mM NaCl, and 1 mM DTT. It is worth noting that even in the presence of high salt conditions, $ELKS1^{\Delta IDR/+P3N}$ and CLIP170 formed droplets during purification. The droplets were collected using centrifugation and was subsequently used for LLPS assays.

Analytical size exclusion chromatography

Protein samples with a volume of 100 μl were prepared at a final concentration of 40 μM and loaded onto an analytical size exclusion column (Superdex 200 Increase 10/300 GL, GE Healthcare) on an ÄKTA pure system (GE Healthcare). The column was pre-equilibrated with the same buffer that was used the protein purification.

Crystallization and X-ray data collection

For crystallization, the freshly purified CLASP2_TOG4 and ELKS2_CC3 proteins were concentrated to ~10 mg/ml and mixing with CENP_CC, CLIP-170_CC, or LL5β_CC and LL5β_EBM at a molar ratio of 1:1.2, respectively. In addition, to ensure the CLASP2_TOG4 forms a stable 1:1 complex with LL5β_TBM during crystallization, the LL5β_TBM sequence was fused to the C-terminus of CLASP2_TOG4 with a thrombin cleavage sequence in between them, resulting in a chimeric protein of $CLASP2\_TOG4^{+LL5\beta\_TBM}$. Crystals were grown by the hanging drop vapor diffusion method at 16 °C in a reservoir solution containing 0.2 M ammonium acetate, 0.1 M Tris pH 8.5, 25% w/v polyethylene glycol (PEG) 3,350 for the Se-Met derivative CLASP2_TOG4 in complex with CLIP170_CC, containing 0.2 M NaCl, 0.1 M Tris pH 8.5, and 25% w/v PEG 3,350 for the native CLASP2_TOG4 in complex with CLIP170_CC, containing 0.2 M NaCl, 0.1 M Bis-Tris pH 5.5, and 25% w/v PEG 3,350 for $CLASP2\_TOG4^{+LL5\beta\_TBM}$, containing 0.2 M $(NH_4)_2SO_4$, 0.1 M Bis-Tris pH 6.5, and 25% w/v PEG 3,350 for the CLASP2_TOG4/LL5β_CC complex, containing 0.1 M HEPES pH 6.5 and 1.4 M sodium citrate for the CLASP2_TOG4/CENP-E_CC complex, or containing 0.2 M ammonium formate pH 6.6 and 20% w/v PEG 3,350 for the ELKS2_CC3/LL5β_EBM complex. Before been stored in liquid nitrogen, the crystals were soaked

in crystallization solution containing additional 25% glycerol for cryoprotection. The diffraction data of the crystals was collected at the beamline BL17U1, BL18U1, and BL19U1 at Shanghai Synchrotron Radiation Facility (SSRF). The data were processed and scaled using HKL2000 [67].

Structure determination and analysis

The structure of CLASP2_TOG4 in complex with CLIP_CC was determined by using single wavelength anomalous diffraction (SAD) phasing in AutoSol [68]. The other structures of CLASP2_TOG4 in complex with its targets were determined by molecular replacement in PHASER [69] using the CLASP2_TOG4 structure as the search model. The coiled-coil structure of the ELKS2-CC3/LL5-EBM complex was solved by combinatorial usage of ARCIMBOLDO_LITE [70] in CCP4 [71] and PHASER. All the structural models were refined in PHENIX [72] and adjusted in COOT [73]. The model quality was check by MolProbity [73]. The final refinement statistics are listed in Table S1. All structure figures were prepared by using PyMOL (https://www.pymol.org).

Isothermal titration calorimetry (ITC)

ITC measurements were performed on a PEAQ-ITC Microcal calorimeter (Malvern). The CLASP2_TOG4 or LL5β_EBM were prepared with a concentration of 200 μM in the syringe and the CLIP170_CC, LL5β_TBM, CENP-E_CC, GCC185_CC or ELKS2_CC3 with a concentration of 20 μM in the cell. All the protein samples were prepared in a buffer containing 50 mM Tris pH 7.5 and 100 mM NaCl. The titration was processed by injecting 3 μl of sample in the syringe to the cell each time. An interval of 150 s between two injections was set to ensure the curve back to the baseline. The titration data were analyzed and fitted by a one-site binding model.

Cell culture and transfection

HeLa cells and HEK 293T were maintained in Dulbecco's Modified Eagle's Medium (DMEM) supplemented with 10% fetal bovine serum (FBS) and 1% penicillin-streptomycin solution and 1% non-essential amino acids. The cells were cultured at 37 °C in an incubator with 5% CO_2. Lipofectamine 3000 reagent (Thermo Fisher Scientific) was used for HeLa and HEK 293T cells transfection, and polyethylenimine linear (PEI) MW40000 (YEASEN) was used for HEK 293F cells transfection.

Immunofluorescence and imaging

Hela cells or HEK293T cells were transfected with constructs and transferred to glass coverslips (treat with 10 mg/ml fibronectin for 1 hour) after 24 hours. Cells grew on glass coverslips for 12h. For nocodazole treatment, 10 μM nocodazole was added into the culture medium for different durations. Cells were fixed with 4% PFA for 15 min at 37 °C or fixed with -20 °C methanol for 10 min at room temperature. After washing with PBS, cells were treated with 0.1% Triton X-100 for 10 min at room temperature, and blocked in 2% Bovine Serum Albumin for 30 min. The cells were stained by primary and secondary antibodies for 1 hour at room temperature. In the condensate attachment assay, the cells were first cultured on glass coverslips (treat with 10 mg/ml fibronectin for 1 hour) and were transfected after 12 hours. The cells were visualized with 100x objective using

Nikon A1R and Zeiss LMS980 Confocal Microscopes. The methods used for image analysis were mentioned in corresponding figure legends.

***In vitro* LLPS assay**

All stock proteins were centrifuged at ~20,000 g for 10 minutes at 4 °C to remove any precipitations and diluted to designed concentrations with a dilution buffer containing 50 mM Tris pH 7.5, 100 mM NaCl, and 1 mM DTT. For protein fluorescence labeling, Cy3 or iFluor 405 NHS ester (AAT Bioquest) were mixed with the corresponding protein at 1:1 ratio in the PBS buffer. The mixture was incubated at room temperature for 1 hour. The reaction was quenched by adding 200 mM Tris pH 7.5. To remove the unlabeled fluorophores, the labeled proteins were exchanged into a buffer containing 50 mM Tris pH 7.5, 150 mM NaCl and 1mM DTT using a desalting column. Fluorescence labeling efficiency was measured by NanoDrop (Thermo Fisher). In fluorescent imaging experiments, fluorescently labeled proteins were mixed with the corresponding unlabeled proteins at 1:50 ratio. Fluorescent images were captured 15 min after the samples were added to a 384-well glass bottom plate (Cellvis). The imaging was conducted using a Nikon A1R Confocal Microscope at room temperature.

siRNA-knockdown

ELKS1, LL5β, CLASP1, and CLASP2 were knocked down in HeLa cells by using siRNA with Lipofectamin 2000 reagent (Invitrogen). Cells were cultivated in 6-well plates prior to transfection. In each well, ELKS1 siRNA [74] (20 pmol), LL5β siRNA [75] (20 pmol), or CLASP1 (20 pmol) and CLASP2 (40 pmol) siRNAs [22], were used. For rescue experiments, cells were co-transfected with 1 μg of DNA per well. Following transfection, fresh medium was replaced every 24 hours. After 60 hours post-transfection, the cells were transferred to glass coverslips that had been treated with 10 mg/ml fibronectin for 1 hour. The cells were then cultured for additional 12 hours before fixation. The excess cells were sampled with a loading buffer and subsequently used for Western blotting.

Live-cell imaging

HeLa cells were transferred to Nunc Glass Base Dish that had been treated with 10 mg/ml fibronectin for 1 hour. A Nikon A1R Confocal Microscope was used for live-cell imaging experiments. Cells were kept in a humidified condition of 5% CO_2 in a 37 °C incubation chamber during the experiments.

Superresolution imaging

To analyze the spatial relationship between the ELKS1 condensate and MTs, Single-molecule localization microscopy (SMLM) was used to image Hela cells transfected with GFP-ELKS1 on the high-precision coverslips (no. 1.5H, CG15XH, Thorlabs). For dual-color staining, GFP-ELKS1 proteins were labeled with anti-GFP nanobodies conjugated Alexa Fluor 647 (FluoTag-Q, N0301-AF647-L, SYSY), and MTs were labeled with anti-β-tubulin (mouse, 1:600, T4026, Sigma) and secondary antibodies conjugated CF680 (anti-mouse, 1:250, 20817, Biotium). For SMLM imaging, samples were immersed in buffer containing 50 mM Tris-HCl (pH 8.0), 10 mM NaCl, 10% (w/v) glucose, 0.5 mg/ml glucose oxidase (G7141, Sigma), 40 μg/ml catalase (C100, Sigma) and 35 mM

cysteamine. SMLM imaging was performed at room temperature on a custom-built microscope. During data acquisition, samples were excited with a 640-nm laser (~ 2 kW/cm^2) and recorded 100,000 frames with 20-ms exposure time and the z-focus stabilized by a customized focus lock system.

The raw dual-color data were global fitted and analyzed with SMAP software as described previously [76]. The global multi-channel experimental PSF model was generated based on the z stacks of beads (T7279, Invitrogen) on a coverslip. The color of single molecules was assigned by the ratio of the intensities in each channel. For sample drift, the x, y and z positions were corrected based on redundant cross-correlation algorithm. The localizations appearing in consecutive frames (within 35 nm) were regarded as a single molecule, and thus merged into one localization. To reject dim localizations and bad fits, localizations were filtered by x-y precision (0-20 nm), z precision (0-45 nm), photon count (> 800) and relative log-likelihood (> -2.5).

Co-immunoprecipitation

Transfected HEK293T cells were lysed in an ice-cold lysis buffer containing 50 mM Tris pH 7.5, 150 mM NaCl, 1% Triton X-100, 5% glycerol, 1 mM phenylmethylsulfonyl fluoride, and protease inhibitor cocktail (TargetMol) for 30 min at 4 °C and followed by a centrifugation at 12000 g for 15 min at 4 °C. After centrifugation, the supernatants were incubated with GFP Nanoab Agarose beads for 1 hour at 4 °C. After washing four times in the lysis buffer, the samples were mixed with the loading buffer, then boiled for 10 min, and examined by western blotting.

Western blotting

The prepared samples were separated by 4-12% SDS-PAGE (GenScript, M41212C) and transferred to polyvinylidene fluoride membrane (Millipore, IPVH00010). The membranes were sequentially blocked with 3% BSA in TBST buffer containing 50 mM Tris-HCl pH 7.4, 150 mM NaCl, and 0.1% Tween 20, immunoblotted with first antibodies, and probed with HRP-linked antibody secondary antibodies, and finally developed with a chemiluminescent substrate (BioRad, 107-5061). After each step, the membranes were washed three times with TBST buffer. Protein bands were visualized on the Tanon-6011C Chemiluminescent Imaging System (Tanon Science and Technology).

Calculation of MT orientation

The initial step involves segmenting the entire single-cell image into four Regions of Interest (ROIs). These ROI images were then subjected to two-dimensional Fourier transform to extract their frequency content. Subsequently, an elliptic feature analysis was conducted to quantitatively evaluate the MT distribution. The anisotropic property of the microtubule fibers is characterized by calculating the ratio of the major axis to the minor axis of the resulting ellipse. The MATLAB software was used for calculation, and the corresponding codes were uploaded to the GitHub website (https://github.com/GuoSiqi350/2D-FT-Elliptic-Feature-Analysis.git).

Statistics and data reproducibility

Image pro plus software and NIS-Elements A1R Analysis software were used to analyzed captured images or movies. Significance was analyzed using an unpaired, two-tailed Student's *t* test model. All the statistical analysis was performed and exported to figures using GraphPad Prism 8.0 and Origin 2019.

Figures

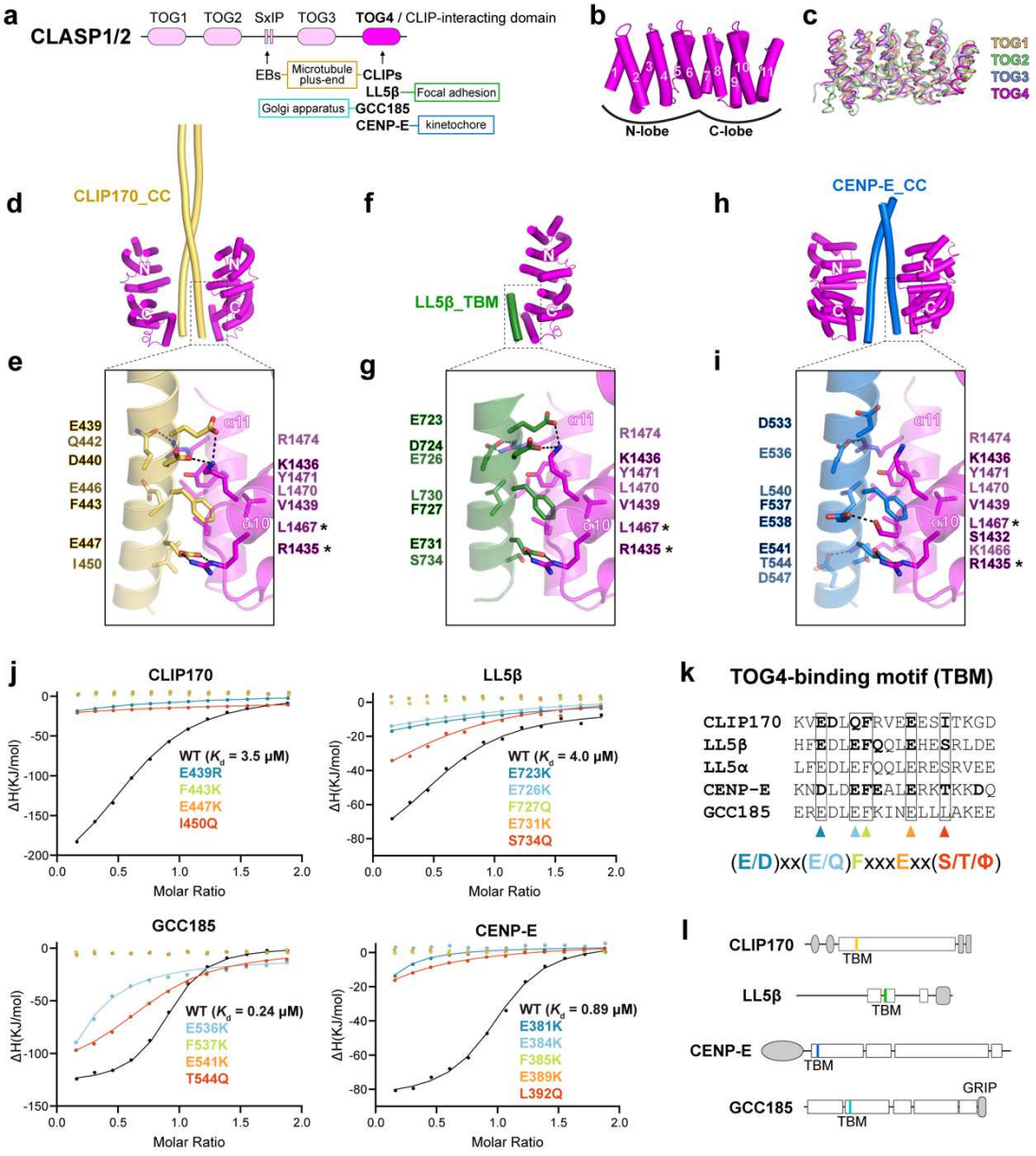

Figure 1. Biochemical and structural characterization of TOG4-binding motifs.

a, Domain organization of CLASP proteins, highlighting the regions responsible for interactions with various binding partners, essential for their cellular targeting.

b, Overall structure of the TOG4 domain in CLASP2, consisting of 11 α-helixes.

c, Structure alignment of the four TOG domains in CLASP2, showing the overall folding similarity. The PDB codes of the TOG1, TOG2, and TOG3 structures are 5NR4, 3WOY, and 3WOZ, respectively.

d-i, Structural analyses of the interactions between the TOG4 domain and its binding fragments in CLIP170 (**d,e**), LL5β (**f,g**), and CENP-E (**h,i**). Overall structures of these complexes are presented in **d**, **f**, and **h**, with detailed interface interactions shown in **e**, **g**, and **i**. Salt bridges and hydrogen bonds are indicated by dashed lines.

j, ITC-based analysis showing the similar interaction mode for TOG4-mediated interactions. Corresponding titration curves are listed in Extended Data Fig. 3.

k, Sequence alignment of the TOG4-binding motifs (TBMs) in human CLIP170, LL5α, LL5β, GCC185 and CENP-E, highlighting the consensus sequence for TOG4 binding. Residues involved in TOG4 binding, as revealed by the structural analyses in **e**, **g**, and **i**, are shown in bold.

l, Domain organizations of CLIP170, LL5β, CENP-E, and GCC185 showing their TBM locations in coiled coils. The coiled-coil regions are colored in white while other domains are colored in grey.

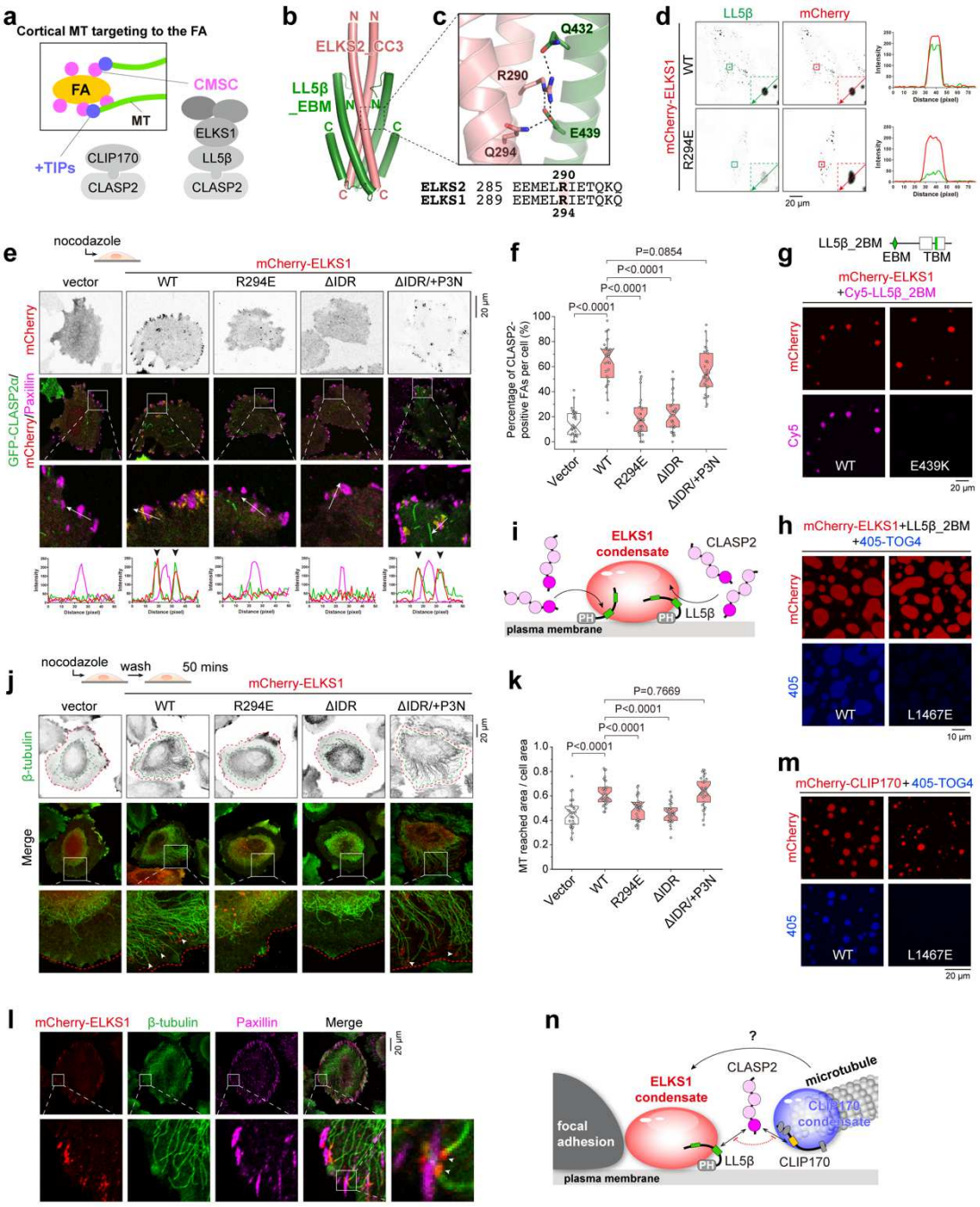

Figure 2. The LLPSs of ELKS1 and CLIP170 facilitate CLASP2 and MT targeting.

a, Schematic model showing the involvement of CLASP2 in two complexes at the MT plus end and FA vicinity for cortical MT targeting.

b, Overall structure of the ELKS2_CC3/LL5β_EBM complex.

c, Molecular details of the interface between ELKS2_CC3 and LL5β_EBM. R290 in ELKS2, corresponding to R294 in ELKS1, forms salt bridges and hydrogen bonds with LL5β_EBM, as indicated by dashed lines.

d, Cell imaging analysis showing the critical role of R294 for the recruitment of endogenous LL5β into the ELKS1 condensate. HeLa cells were transfected with mCherry-tagged ELKS1 or its R294E mutant. Cells were fixed and stained with anti-LL5β antibody.

e, Cellular analysis of CLASP2 accumulation at the FA vicinity. HeLa cells were co-transfected with GFP-tagged CLASP2α with mCherry-tagged ELKS1 or its mutants. Cells were treated with 10 μM nocodazole for 2 hours before fixation. FAs were stained by anti-Paxillin antibody. The CLASP2 distribution at the FA vicinity is further indicated by arrowheads in line analysis.

f, Quantification of the percentage of FAs with CLASP2α clusters at their vicinity as shown in **e**. The paxillin-stained FAs (> 0.3 μm^2) were selected for statistics. Data are mean ± s.d. (n = 30 cells).

g, *In vitro* co-phase separation of mCherry-ELKS1 and Cy5-labeled LL5β_2BM. The protein concentration used in this assay was 5 μM for both ELKS1 and LL5β fragments.

h, *In vitro* co-phase separation of mCherry-ELKS1, LL5β_2BM, and 405-labeled CLASP2_TOG4 or its TBM-binding deficient mutant. The protein concentration used in this assay was 10 μM for all proteins.

i, A schematic model illustrating the cortical ELKS1/LL5β co-condensate recruiting CLASP2 via LLPS.

j, Cell imaging of cortical MT targeting in nocodazole-treated cells. HeLa cells were transfected with mCherry, mCherry-tagged ELKS1, or its mutants. After being treated with 10 μM nocodazole for 2 hours, transfected cells were washed three times and cultured in the fresh medium for 50 mins. MTs were stained by anti-β-tubulin antibody. Cell edges and MT reaching boundaries are indicated by red and green dashed lines. ELKS1 puncta at MT tips are indicated by arrowheads in zoom-in views.

k, Quantification of the proportion of MT reaching area to the total cell area as shown in **j**. Data are mean ± s.d. (n=30 cells)

l, Cell imaging of ELKS1 condensates at the FA vicinity. Transfected cells were treated using the same procedure as in **a**. FAs were stained by anti-paxillin antibody.

m, *In vitro* co-phase separation of mCherry-CLIP170 and 405-labeled TOG4 or its TBM-binding deficient mutant.

n, A schematic model illustrating the multiphase system in MT targeting, involving the ELKS1 and CLIP170 condensates.

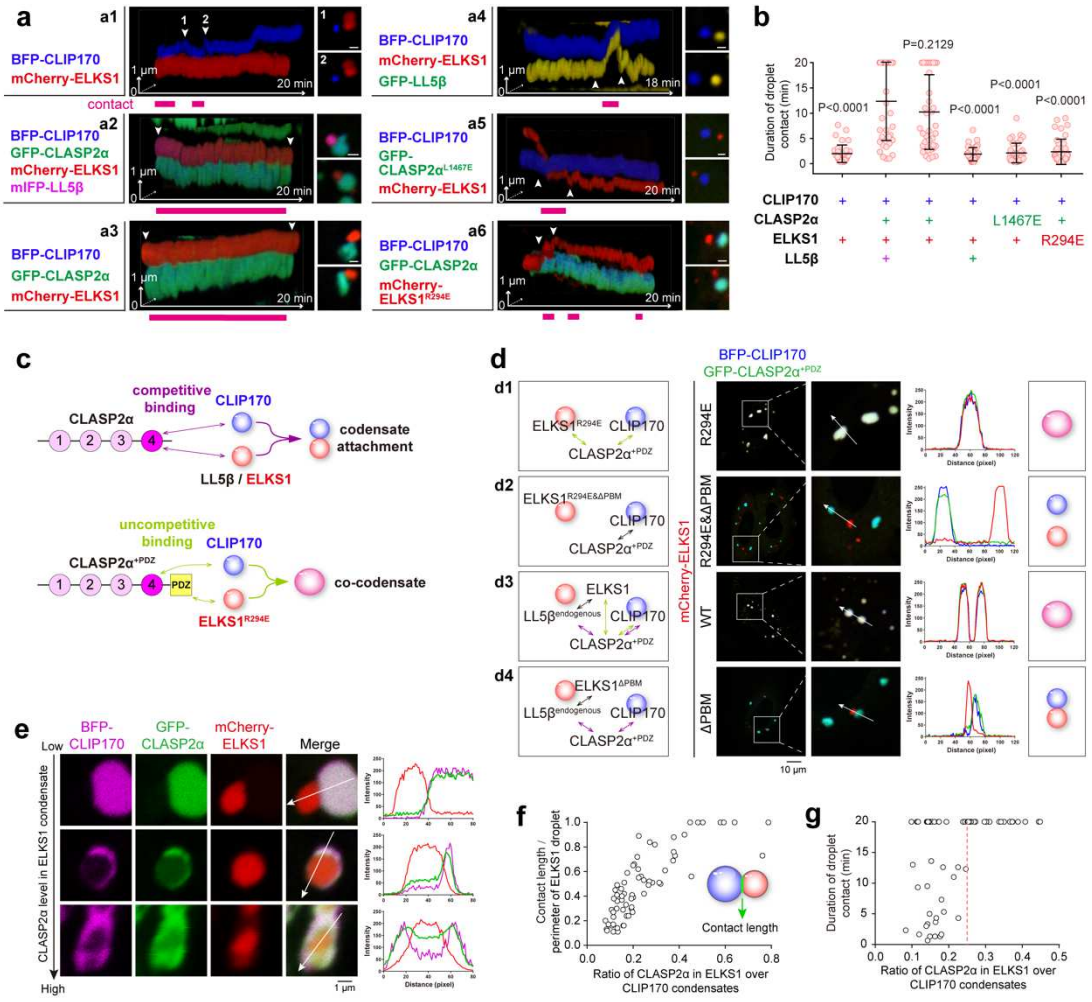

Figure 3. Competitive binding to CLASP2 in the condensed phase mediates condensate attachment.

a, Kymographic analysis of attachment between the ELKS1 and CLIP170 condensates. Kymographs were generated using NIS-Elements A1R Analysis software. The magenta lines indicate the contact duration between the two types of droplets. The upper limit of recording time was set to 20 mins. Two snapshots indicated by arrowheads in each kymography are shown aside. See also Extended Data Movie 1.

b, Quantification of the contact duration between the ELKS1 and CLIP170 droplets as indicated in **a**. Data are mean ± s.d. (n = 40 droplet contacts from 10 movies).

c, Schematic models of condensate interactions mediated by CLASP2α. Competitive binding to CLASP2α leads to condensate attachment, while introducing uncompetitive binding to CLASP2α^{+PDZ} results in co-condensate formation.

d, Cellular analysis of the effect of competitive binding on condensate interactions. The designed interactions and outcomes are illustrated in the corresponding left and right diagrams, respectively.

e, Droplet contact analysis of the ELKS1 condensate with varying CLASP2 levels. To alter the CLASP2 level in the ELKS1 condensate, the plasmid ratios of CLIP170, CLASP2α, and ELKS1 transfected into cells were set as 1:1:1, 1:2:1, and 1:3:1.

f, Scatterplot of the contact levels of CLIP170 droplets on ELKS1 droplets with different CLASP2 levels. The corresponding contact levels at different CLASP2 levels in the ELKS1 condensate were calculated from a total of 68 droplet contacts.

g, Scatterplot of the contact duration between the ELKS1 and CLIP170 droplets with different CLASP2 levels in the ELKS1 condensate. A total of 65 droplet contacts from 20 movies were recorded. See also Extended Data Fig. 9g for examples.

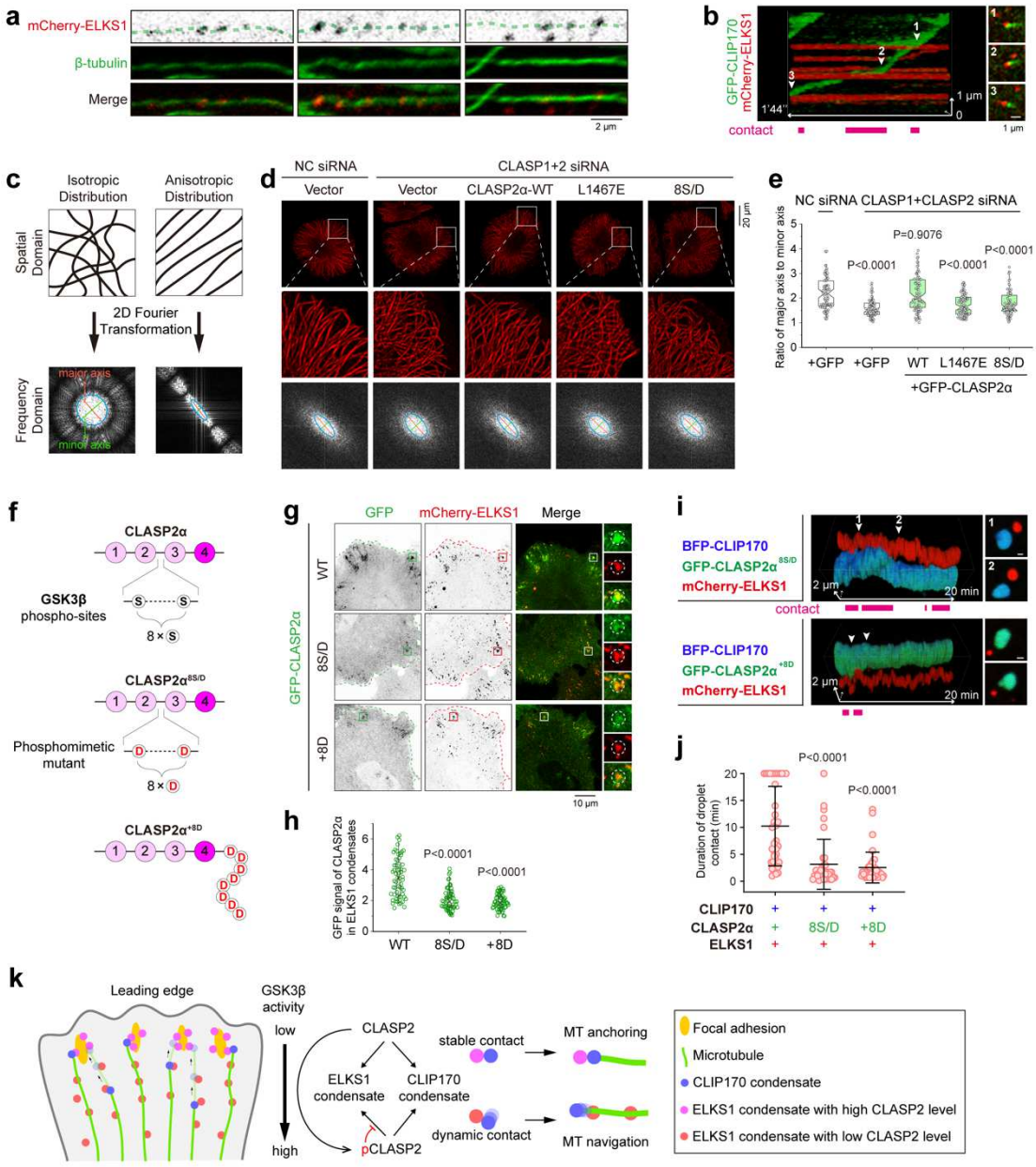

Figure 4. Phosphorylation of CLASP2 regulates condensate attachment for cortical MT organization.

a, Distribution of ELKS1 condensates along MTs. Cellular regions with less dense of MTs were chosen for imaging.

b, Kymographic analysis showing the MT plus end with the CLIP170 condensate passing through multiple ELKS1 condensates. Three snapshots indicated by arrowheads in the kymography are shown aside. See also Extended Data Movie 3.

c, Schematic diagrams illustrating the quantitative evaluation of MT distribution patterns by applying 2D Fourier transformation.

d, Cellular analysis of cortical MT organization regulated by CLASP2. Cells were fixed with methanol at -20 °C. 2D Fourier transform was applied to MT patterns of different samples, and corresponding results were shown at the bottom.

e, Quantification of the ratio of the major axis to the minor axis for the ellipses in the frequency domain as shown in the bottom panels in **d**. Four regions near the cell edge in each cell were selected as the ROIs. Data are mean ± s.d. (n = 20 cells).

f, Schematic diagrams illustrating the phosphomimetic mutation (8S/D) in CLASP2α.

g, Cell imaging of the accumulation of CLASP2α in the ELKS1 condensate in cells. The ROIs containing the cortical ELKS1 condensate are indicated by dashed circles.

h, Quantification of the GFP signal of CLASP2α in the ROI as shown in **g**. Three ROIs containing the cortical ELKS1 condensate were randomly selected for each cell. The GFP signal was normalized to background fluorescence intensity. Data are mean ± s.d. (n = 20 cells).

i, Kymographic analysis of the weakened attachment between the ELKS1 and CLIP170 condensates in cells overexpressing CLASP2α mutants. See also movie S4.

j, Quantification of the contact duration between the ELKS1 and CLIP170 droplets as indicated in **i**. Data are mean ± s.d. (n = 40 droplet contacts from 10 movies).

k, A schematic model illustrating cortical MT organization mediated by CLASP2. The different levels of CLASP2 in the condensed phase, which are regulated by GSK3β-dependent phosphorylation, determine the two different modes of condensate attachment for MT anchoring and navigation.

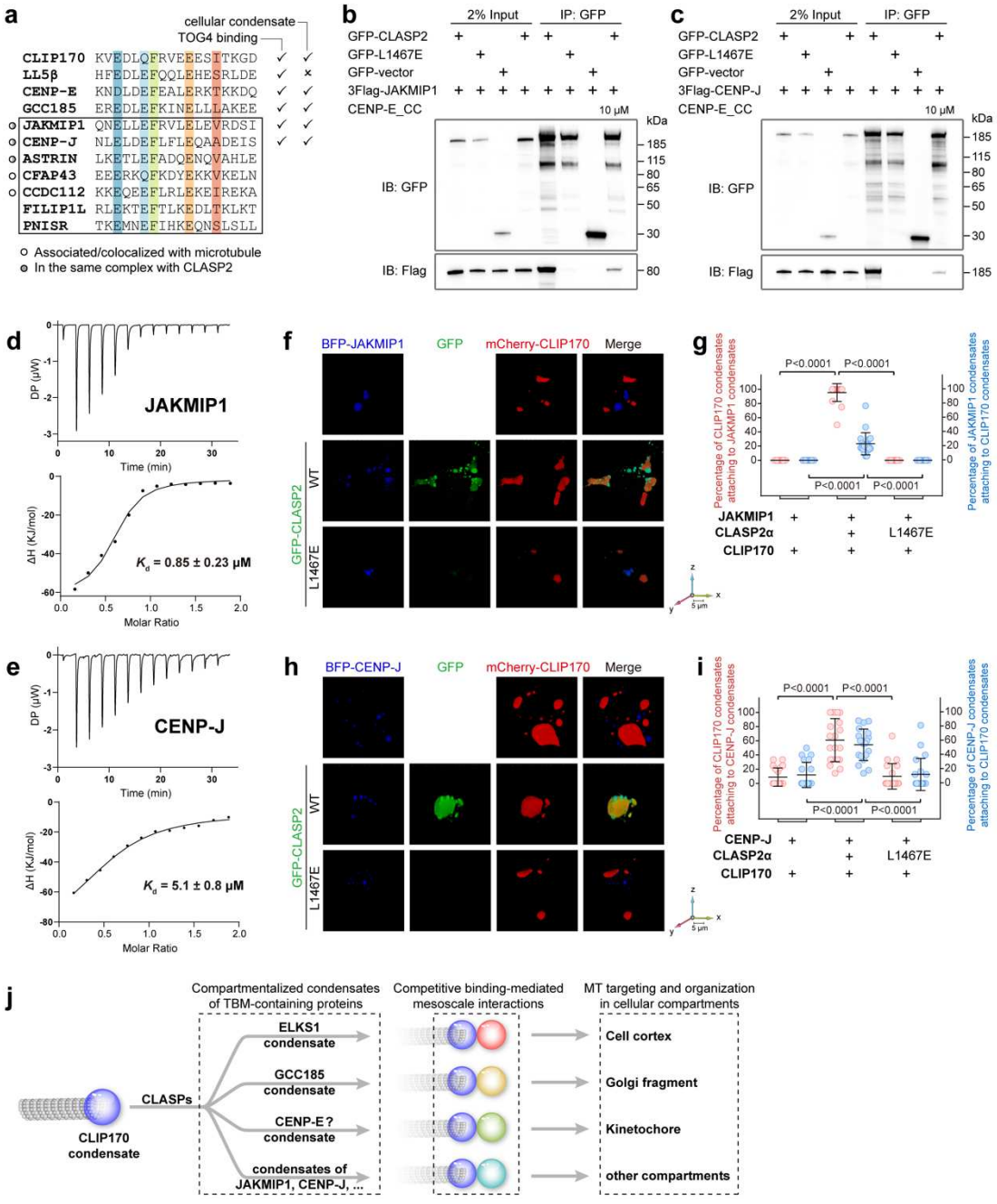

Figure 5. CLASP2 mediates condensate attachment in other TBM-containing proteins.

a, Sequence alignment of TBM-containing proteins in the human genome. To identify more TBM-containing proteins *in silico*, a motif search was performed in the Scansite website (https://scansite4.mit.edu/) with the consensus sequence pattern of TBM (Fig. 1M). The helical conformation of the potential TBMs in candidate proteins was checked using AlphaFold2-based predictions (https://www.alphafold.ebi.ac.uk). The newly identified TBM-containing proteins are boxed.

b and **c,** Co-immunoprecipitation assays showing the TOG4-mediated interaction between CLASP2α and JAKMIP1 (**b**) or CENP-J (**c**).

d and **e,** ITC-based analyses of the interaction between CLASP2_TOG4 and TBM-containing fragments in JAKMIP1 (**d**) or CENP-J (**e**). The boundaries used are residues 549 – 627 for JAKMIP1 and residues 571 – 589 for CENP-J.

f-i, Three-dimensional reconstruction (**f, h**) and quantification analysis (**g, i**) of attachment between the CLIP170 and JAKMIP1 (**f, g**) or BFP-CENP-J (**h, i**) condensates. Competitive binding to CLASP2 is required for the condensate interactions, as the L1467E mutation in CLASP2α abolished condensate attachment. Images were captured every 0.2 μm on the Z-axis, and the number of images depended on the distribution of condensates along the Z-axis. The 3D pictures for each cell were generated using NIS-Elements A1R Analysis software. Data are mean ± s.d. (n = 20 cells).

j, A schematic model illustrating TBM-containing proteins in MT organization in various cellular compartments. CLASP2 promotes condensate attachment by mediating mesoscale protein-protein interactions in the condensed phase.

Extended Data Figures

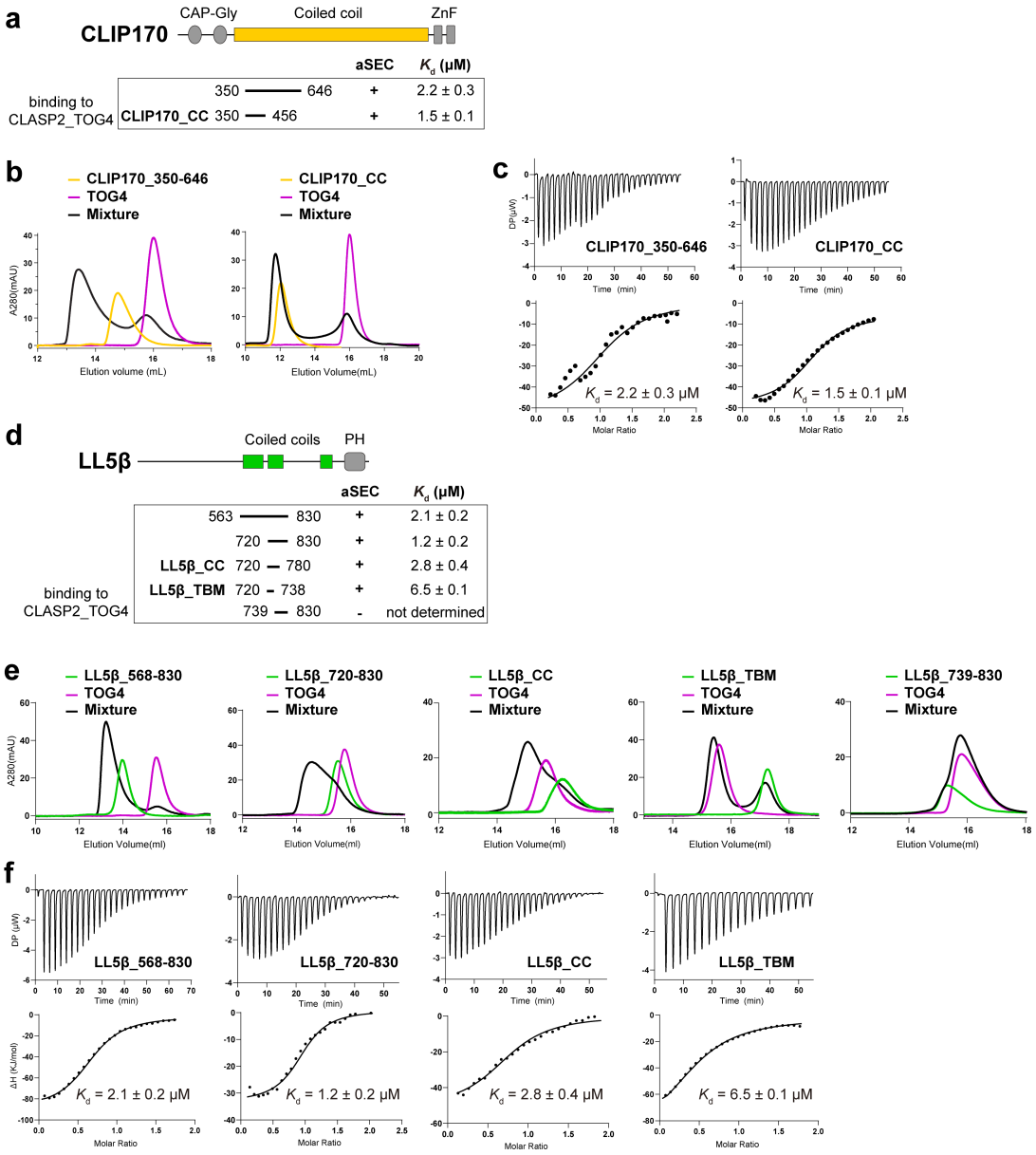

Extended Data Figure 1. Mapping and analysis of the TOG4-binding regions in CLIP170 and LL5β.

a, Domain organizations of CLIP170, indicating the fragments used in this study to identify minimal CLASP-binding sites.

b and **c,** Biochemical analyses of the interaction between CLIP170 and CLASP2_TOG4 with different boundaries using aSEC **(a)** and ITC **(b)**.

d, Domain organizations of LL5β, indicating the fragments used in this study to identify minimal CLASP-binding sites.

e and **f,** Biochemical analyses of the interaction between LL5β and CLASP2_TOG4 with different boundaries using aSEC **(e)** and ITC **(f)**.

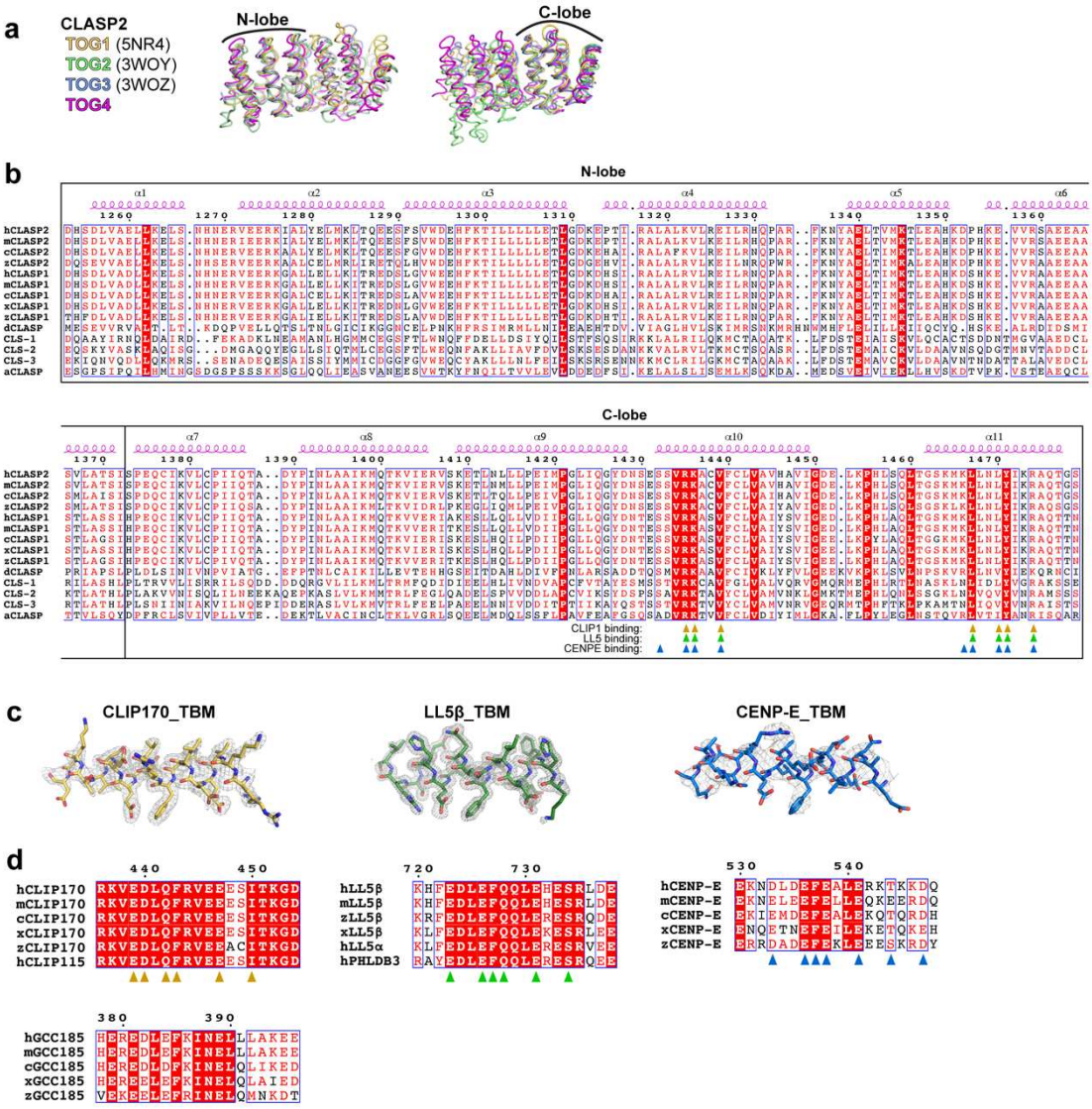

Extended Data Figure 2. Structural and biochemical characterization of the TOG4/TBM interaction.

a, Structural alignment of N-lobe and the C-lobe in TOG domains of CLASP. The PDB codes of the TOG1, TOG2, and TOG3 structures are indicated in parentheses.

b, Amino acid sequence alignments of the TOG4 domains from CLASPs across different species. The prefixes ‘h’, ‘m’, ‘c’, ‘x’, ‘z’, ‘d’, and ‘a’ represent human, mouse, chicken, xenopus, zebrafish, *Drosophila*, and *Arabidopsis*. CLS-1, 2, and 3 are three CLASP homologs in *C. elegans*. The alignment was performed using the ESPript website (https://espript.ibcp.fr/ESPript/ESPript/).

c, $2F_o$-F_c composite omit maps for the TBM fragments of CLIP170, LL5β, and CENP-E with corresponding atomic models superimposed.

d, Amino acid sequence alignments of the TBM sequences in CLIPs (CLIP170 and CLIP115), LL5s (LL5β and LL5α), CENP-E, and GCC185. Residues involved in the interaction with CLASP2_TOG4 are indicated by triangles.

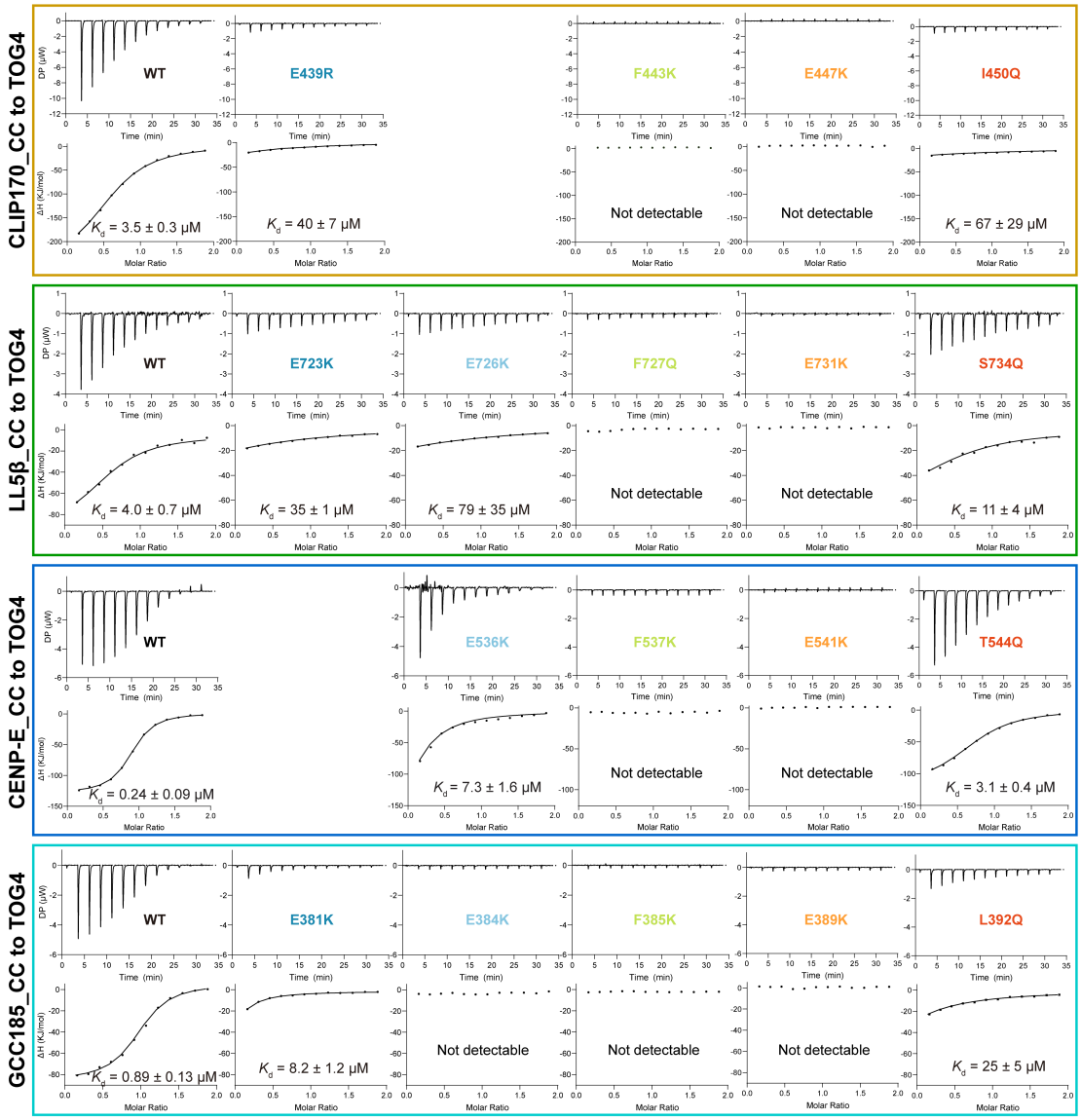

Extended Data Figure 3. ITC-based analyses of the interactions between CLASP2_TOG4 and TBM-containing proteins.

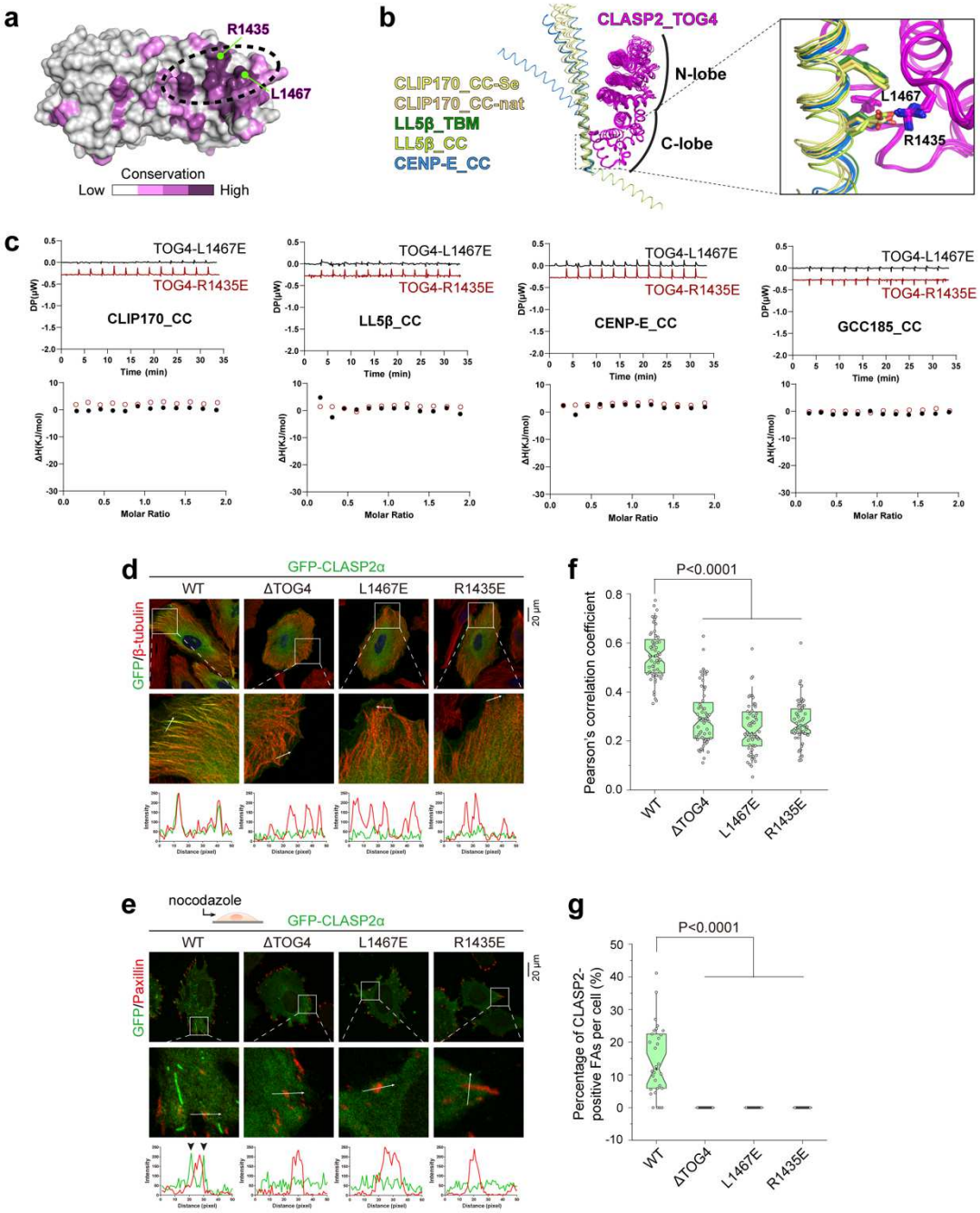

Extended Data Figure 4. The TOG4-mediated interactions and their role in cellular targeting of CLASP2.

a, Surface conservation analysis of the TOG4 domain. The TBM-binding groove is indicated by a dashed circle.

b, Structural alignment of the TOG4 structures in complex with the fragments of CLIP170, LL5β, and CENP-E. The structures were aligned based on the C-lobe of TOG4. As the crystal structures of TOG4 in complex with native and Se-Met derivative CLIP170_CC have different crystal forms, they were both used for the analysis. Molecular details of aligned interfaces between TOG4 and TBMs are shown as an enlarged view. Remarkably, L1467 and R1435 in the TBM-binding groove interact with the two conserved F and E residues in the TBMs, respectively. These two conserved residues are marked in **a**.

c, ITC-based analysis of the abolished binding of TBMs to the L1467E and R1435E mutants of TOG4.

d and **e,** Cell imaging depicting TOG4-mediated localization of CLASP2 in cortical MTs (**d**) and FAs (**e**). HeLa cells were transfected with GFP-tagged CLASP2α or its mutants. To enhance CLASP2 localization at the FA vicinity, cells were pre-treated with 10 μM nocodazole for 2 hours before fixation. FAs were stained by anti-paxillin antibody. The CLASP2 distribution at the FA vicinity is further indicated by arrowheads in line analysis.

f and **g,** Quantitative analyses of CLASP2 localization at the MT tip (**f**) and FA vicinity (**g**). Pearson's correlation coefficient of CLASP2α and tubulin signals as shown in **C** was calculated for 40 regions of interest (ROIs) from 20 cells. The percentage of FAs with CLASP2α clusters in their vicinity, as shown in **e**, was calculated. The paxillin-stained FAs (> 0.3 μm^2) were selected for statistics. Data are mean ± s.d. (n= 30 cells).

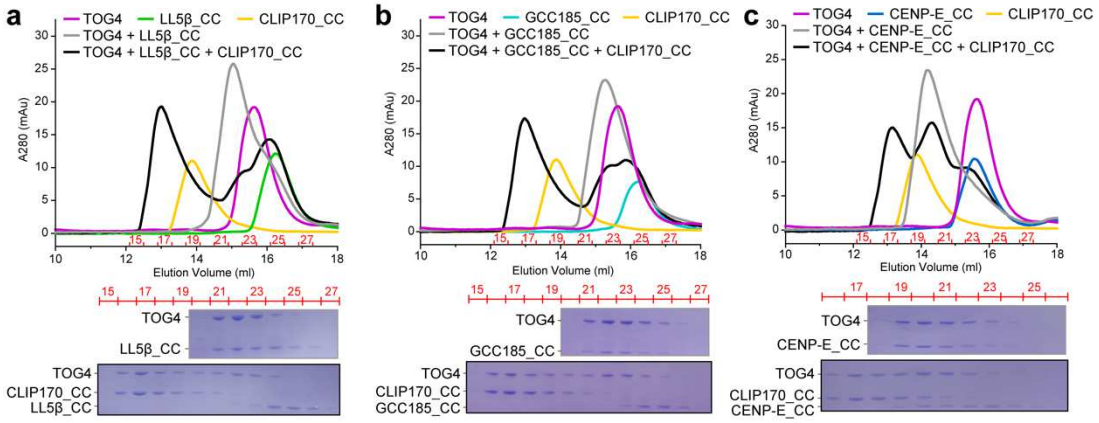

Extended Data Figure 5. TBM-containing proteins compete for the binding to the TOG4 domain of CLASP2.

aSEC-based analysis showed that CLIP170 compete with LL5β (**a**), GCC185 (**b**), and CENP-E (**c**) for CLASP2_TOG4 binding in solution.

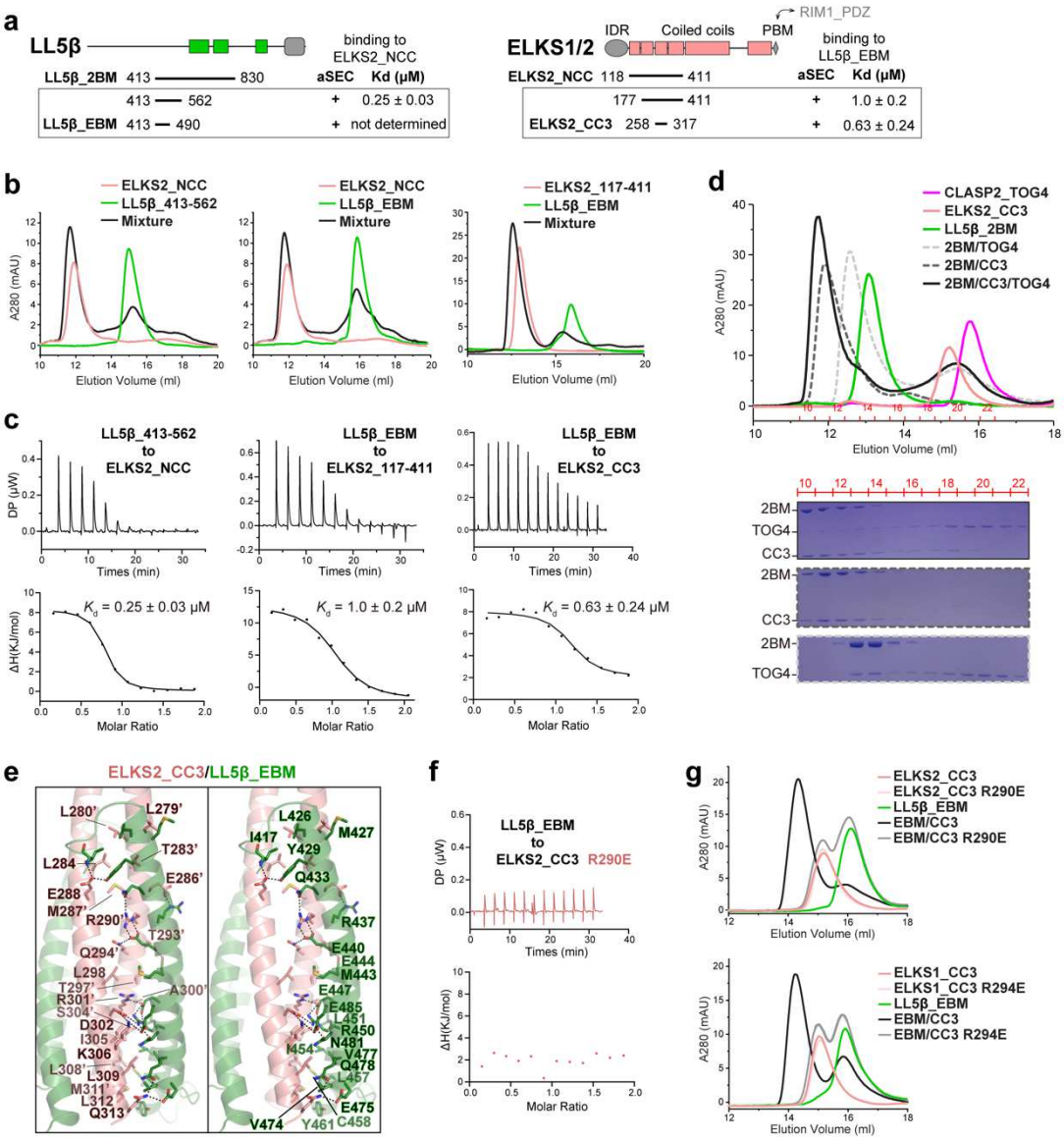

Extended Data Figure 6. Biochemical and structural analyses of the interaction between ELKS2 and LL5β.

a, Domain organizations of LL5β and ELKS proteins, showing fragments of LL5β and ELKS2 used in this study for mapping minimal interacting regions.

b and **c,** The interactions between ELKS2 and LL5β with different boundaries were analyzed by using aSEC (**b**) and ITC (**c**).

d, aSEC-based analysis of a tripartite complex formation of LL5β with CLASP2 and ELKS2.

e, Molecular details of the interface between ELKS2_CC3 and LL5β_EBM. Salt bridges and hydrogen bonds are indicated by dashed lines.

f, ITC-based analysis of the interaction between ELKS2_CC3 R290E mutant and LL5β_EBM.

g, aSEC-based analysis of the interaction between the CC3 fragment of ELKS variants and LL5β_EBM.

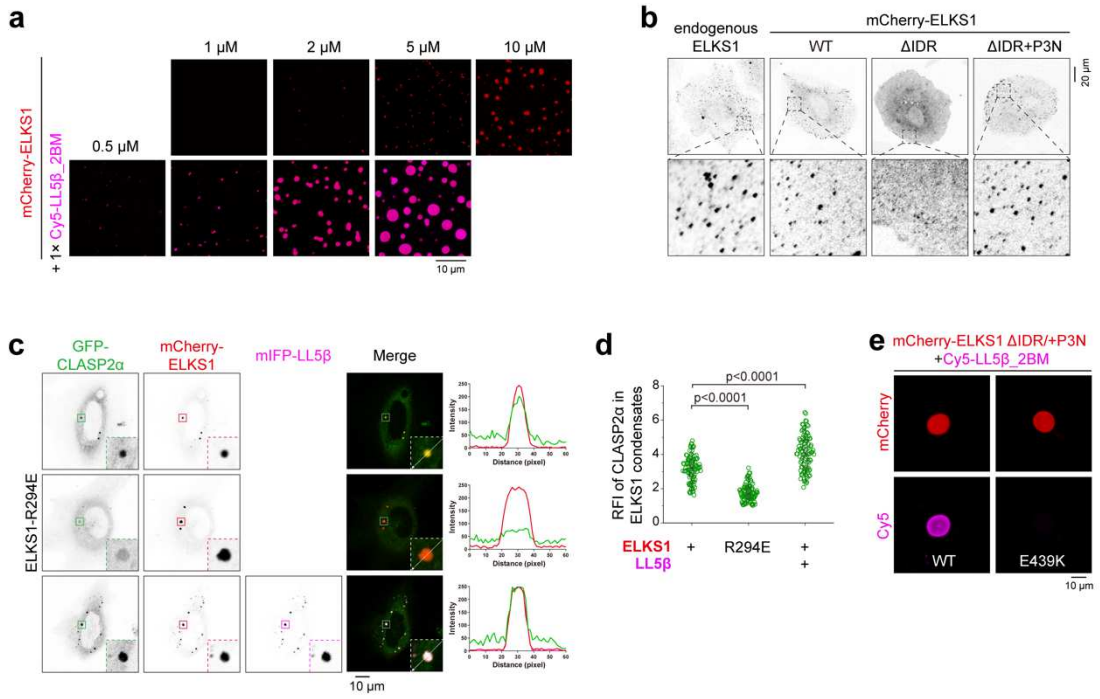

Extended Data Figure 7. ELKS1 recruits LL5β into its condensates.

a, *In vitro* phase separation of purified mCherry-tagged ELKS1 with or without Cy5-labeled LL5β_2BM.

b, Cell imaging of cellular condensate formation of endogenous or overexpressed ELKS1 and its variants.

c, Cell imaging of the ELKS1 condensate in recruiting LL5β and CLASP2. The accumulation levels of LL5β and CLASP2 in the ELKS1 condensate are indicated by line analysis.

d, Quantification of the relative fluorescence intensity (RFI) of CLASP2α in the ELKS1 condensate as indicated in **c**. The RFI was normalized to background fluorescence intensity. Data are mean ± s.d. (n = 100 condensates from 20 cells).

e, *In vitro* co-phase separation of mCherry-ELKS1 ΔIDR/+P3N and Cy5-LL5β_2BM or its ELSK-binding deficient mutant. The protein concentration used in this assay was 5 μM for both ELKS1 and LL5β fragments.

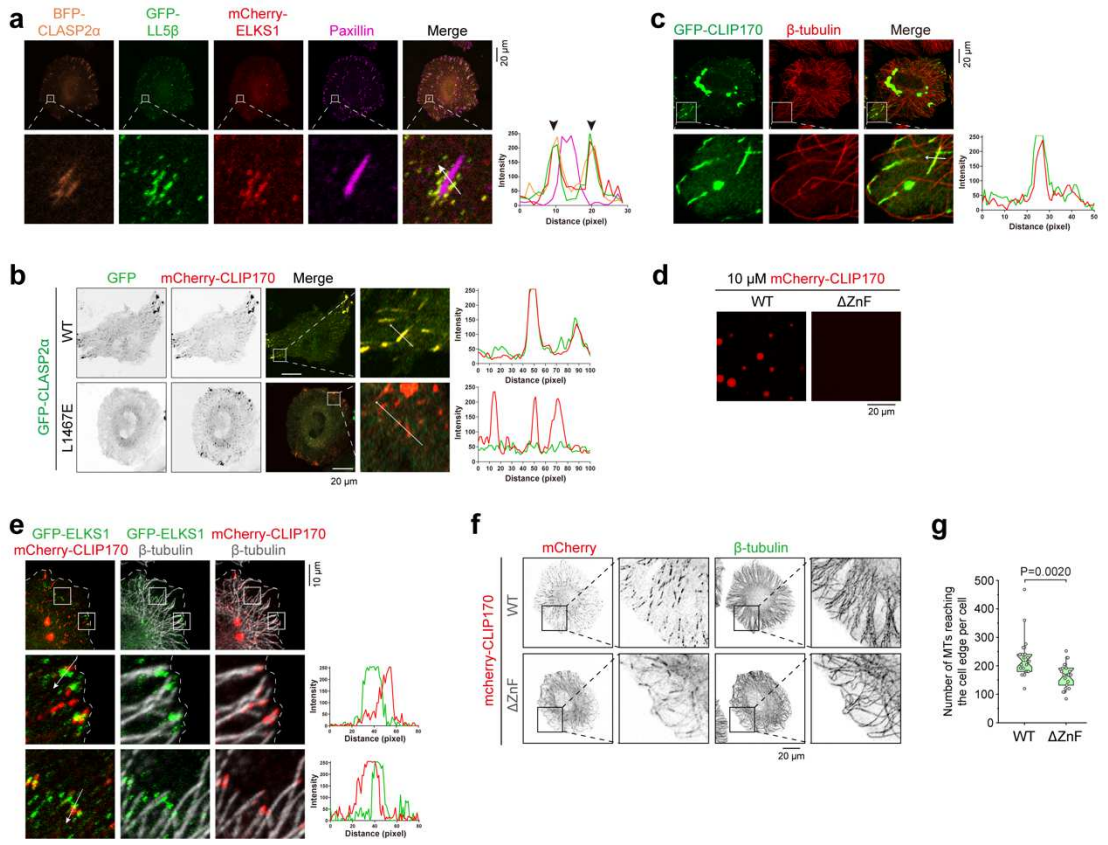

Extended Data Figure 8. The CLIP condensate in targeting CLASP2 and MTs.

a, Cell imaging of CLASP2 in colocalization with its binding proteins at the FA vicinity. The colocalization of CLASP2 with CLIP170 and with LL5β and ELKS1 is further indicated by line analyses.

b, Cell imaging of colocalization of CLIP170 and CLASP2α. Line analysis results of ELKS1 condensates are shown aside.

c, Cell imaging showing CLIP170 condensates on MTs. Line analysis result of a CLIP170 condensate wrapping around a MT is shown aside.

d, *In vitro* phase separation of purified mCherry-tagged CLIP170 and its mutant.

e, Cell imaging showing the spatial relationship between the ELKS1 and CLIP170 condensates at the cell cortex. The non-overlapping positions of the two types of condensates were indicated by line analysis.

f, Cell imaging of cortical MT organization in HeLa cells overexpressing CLIP170 and its mutant.

g, Quantification of the number of MTs reaching the cell edge as indicated in **f**. The regions within 5 μm from the cell edge for 20 cells was used for calculation. Data are mean ± s.d. (n = 20 cells).

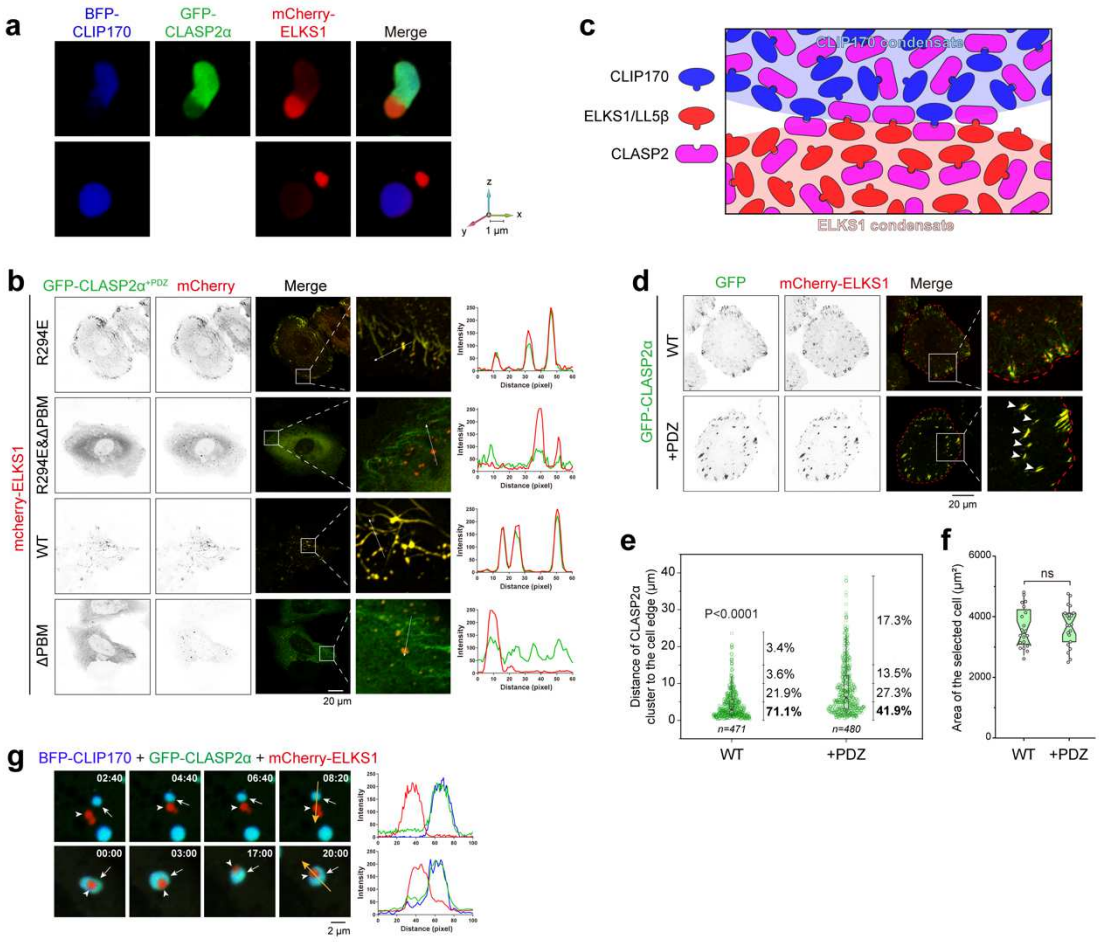

Extended Data Figure 9. Competitive binding to CLASP2α mediates the attachment of the ELKS1 and CLIP170 condensates in cells.

a, Three-dimensional reconstruction of the ELKS1 and CLIP170 condensates in HeLa cells with or without overexpression of CLASP2α.

b, Cell imaging of ELKS1 and its mutants in HeLa cells co-transfected with CLASP2α^{+PDZ}. Line analysis results of ELKS1 condensates were shown aside.

c, A cartoon model of mesoscale protein-protein interactions in the attached interface between the ELKS1 and CLIP170 condensates. The multiple TOG4-binding sites on the surface of condensates allow competitive binding mediated by CLASP2 to facilitate the association between two condensates.

d, Cell imaging showing the altered distribution of the ELKS1 condensate by overexpressing CLASP2α^{+PDZ}. ELKS1 puncta distal to the cell edge are indicated by arrowheads.

e, Quantification of the distance of CLASP2α cluster to the cell edge as indicated in **d**. Data are mean ± s.d. (n = 471 and 480 clusters). 20 cells for each condition.

f, Quantification of cell areas from selected cells in **e**. Data are mean ± s.d. (n = 20 cells).

g, Example snapshots in movies showing the CLASP2-mediated condensate attachment. Line analysis results were performed to indicate CLASP2 levels in condensates.

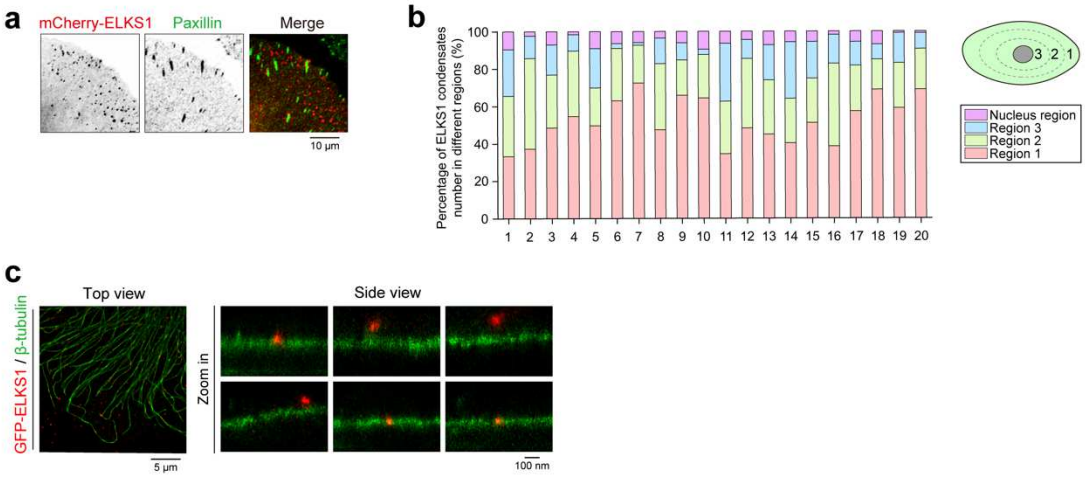

Extended Data Figure 10. Cellular distribution of the ELKS1 condensate.

a, Cellular localization of ELKS1 condensates. FAs were stained by anti-paxillin antibody.

b, The distribution of ELKS1 condensates in each cell. 20 cells with low expression of mCherry-ELKS1 were selected for analysis.

c, Superresolution microscopic analysis of the spatial relationship of the ELKS1 condensate and MTs in HeLa cells.

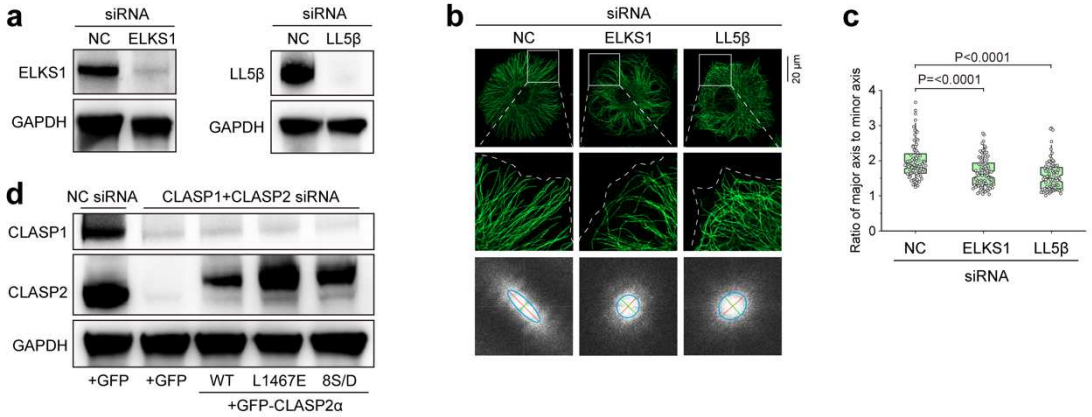

Extended Data Figure 11. Disruption of cortical MT organization by depleting ELKS1, LL5β, or CLASPs.

a, Validation of knock-down efficiency of ELKS1 and LL5β by western blot.

b, Cellular analysis of cortical MT organization of HeLa cells with ELKS1 or LL5β knock-down. Cells were fixed with -20 ℃ methanol. MT was stained by anti-β tubulin antibody.

c, Quantification of the ratio of the major axis to the minor axis for the ellipses as shown in the bottom panels of **b**. Four regions near the cell edge for each cell were chosen as the ROIs, as shown in the enlarged sections in **b**. Data are mean ± s.d. (n = 20 cells).

d, Validation of CLASP1 and CLASP2 double knock-down efficiency by western blot.

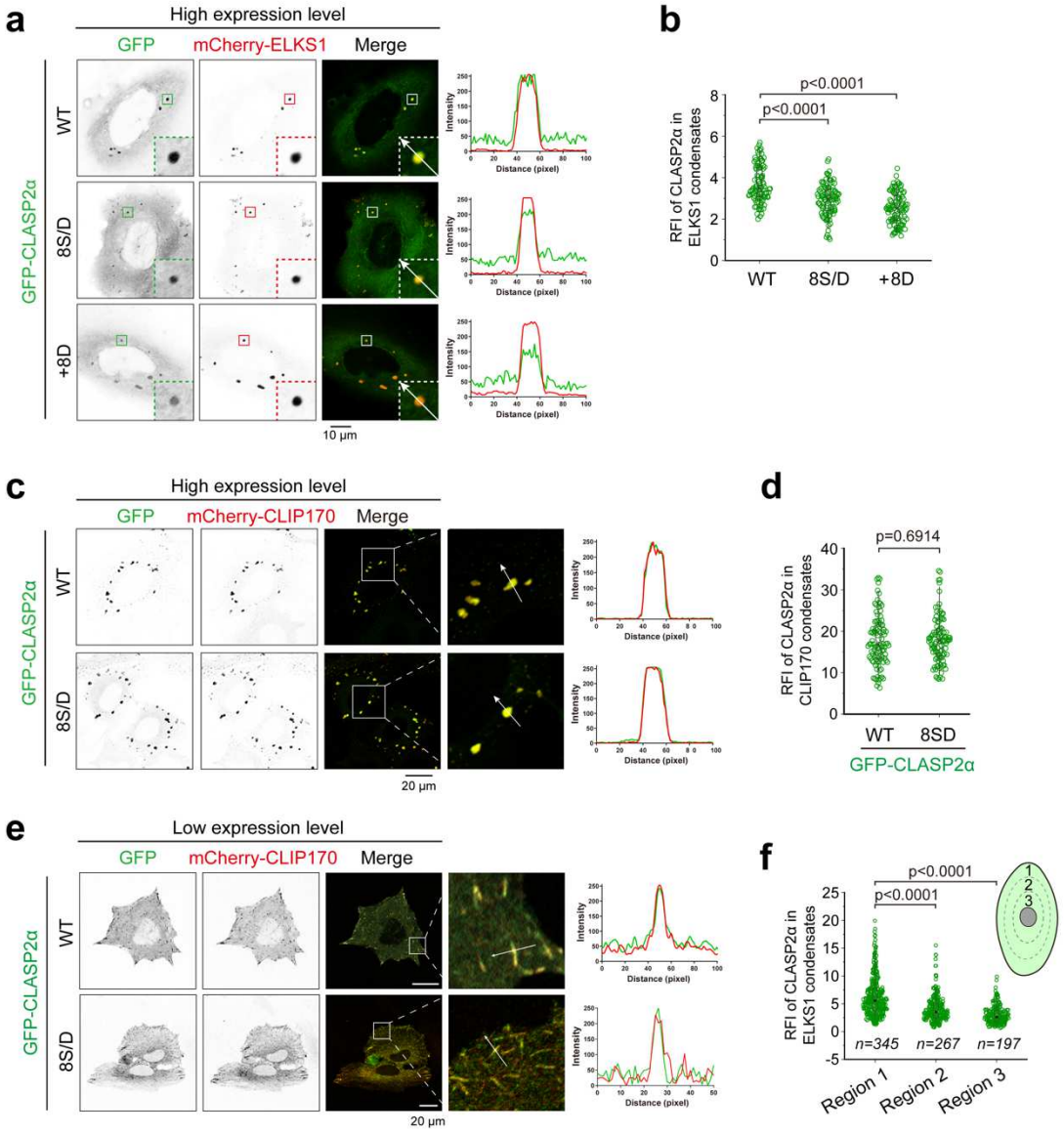

Extended Data Figure 12. Cellular analyses of the charge impact on CLASP2 accumulation in different condensates.

a, Cell imaging of the accumulation of CLASP2α in the ELKS1 condensate in cells with the high expression level of CLASP2α. Line analysis was performed to indicate the change of CLASP2α levels in the ELKS1 condensate.

b, Quantification of the RFI of CLASP2α in the ELKS1 condensate as shown in **a**. The RFI was normalized to background fluorescence intensity. Data are mean ± s.d. (n = 100 condensates from 20 cells).

c, Cell imaging of the accumulation of CLASP2α or its 8S/D mutant in the CLIP170 condensate in cells with high overexpression levels.

d, Quantification of the RFI of CLASP2α in the CLIP170 condensate as shown in **c**. The RFI was normalized to background fluorescence intensity. Data are mean ± s.d. (n=100 condensates from 20 cells).

e, Cell imaging of the accumulation of CLASP2α or its 8S/D mutant in the CLIP170 condensate in cells with low overexpression levels. The majority of CLIP170 condensates localized at the MT plus end.

f, Quantification of the RFI of CLASP2α in the ELKS1 condensate in cells that co-expressed GFP-CLASP2α and mCherry-ELKS1. The cells with relatively low overexpression levels were selected for statistics. Each cell was divided into three regions from the edge to the interior, as shown in the diagram. The RFI was normalized to background fluorescence intensity. Data are mean ± s.d. (n = 345, 267, and 197 condensates at the regions 1, 2, and 3, respectively).

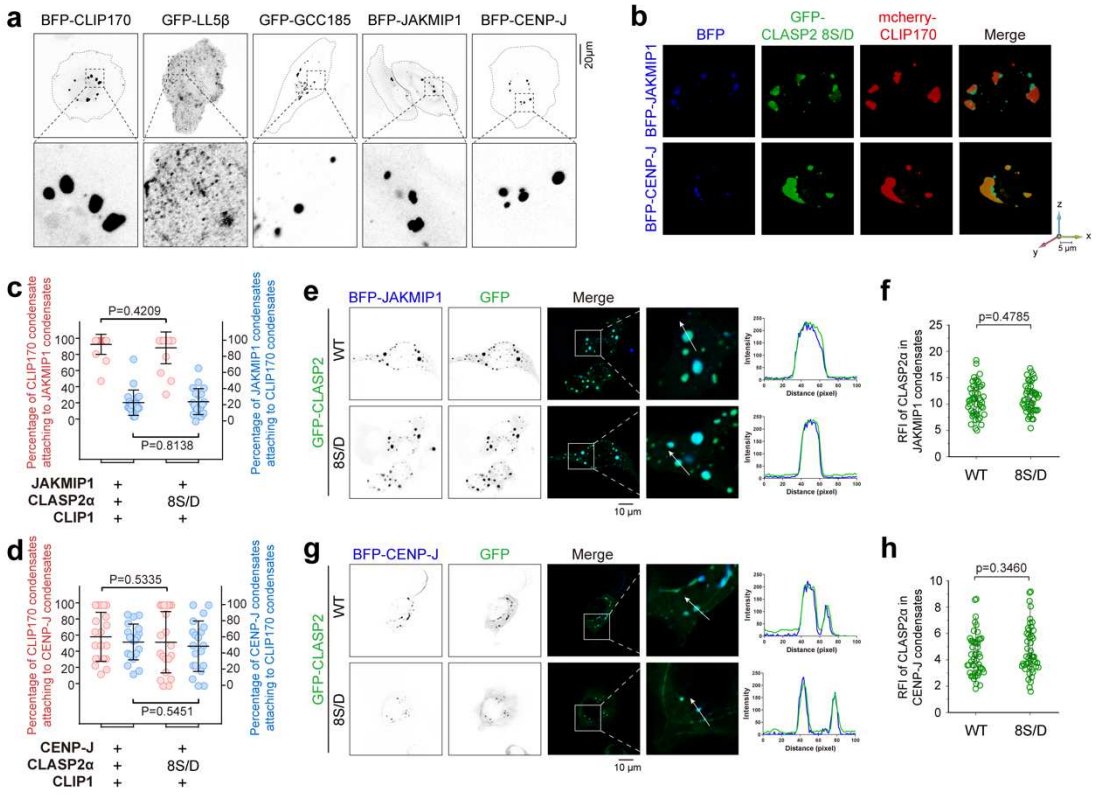

Extended Data Figure 13. Condensate formation and attachment observed in other TBM-containing proteins.

a, Condensate formation in HeLa cells overexpressing indicated TBM-containing proteins.

b-d, Three-dimensional reconstruction (**b**) and quantification analysis (**c, d**) of attachment between the CLIP170 and JAKMIP1 or CENP-J condensates in cells co-transfected with CLASP2α$^{8S/D}$. Images were captured every 0.2 μm on the Z-axis, and the number of images depended on the distribution of condensates along the Z-axis. The 3D pictures were generated using NIS-Elements A1R Analysis software. Data are mean ± s.d. (n = 20 cells).

e-h, Cell imaging (**e, g**) and quantification analysis (**f, h**) of the accumulation of CLASP2α$^{8S/D}$ in JAKMIP1 (**e, f**) or CENP-J (**g, h**) condensates. The RFI was normalized to background fluorescence intensity. Data are mean ± s.d. (n = 50 condensates from 10 cells).

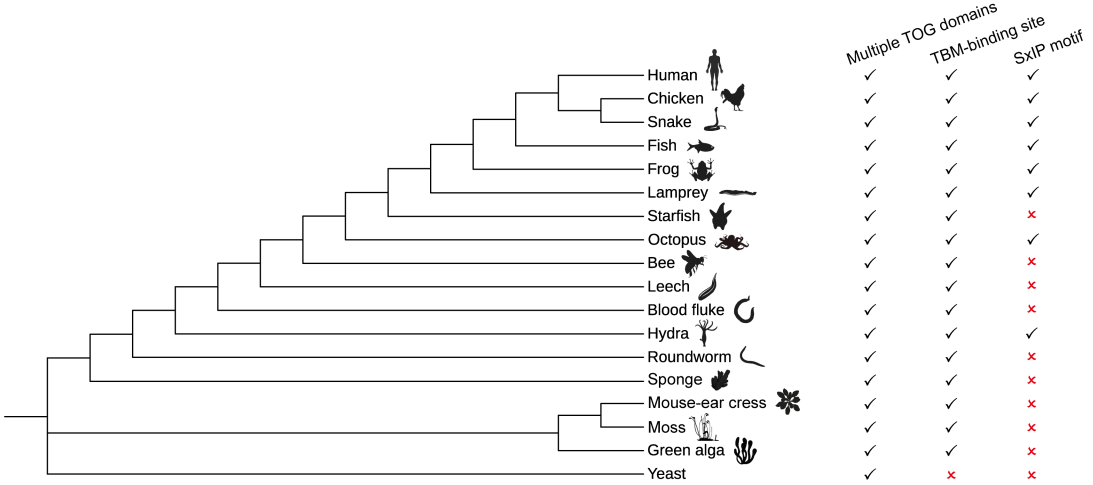

Extended Data Figure 14. Phylogenetic tree for CLASP orthologs.

Protein sequences were obtained from Uniprot (https://www.uniprot.org) with entry ID of O75122 (human), A0A3Q2U2T5 (chicken), A0A670ZBI2 (snake), F1R253 (fish), A1A5G0 (frog), S4REZ4 (lamprey), A0A8B7ZTB8 (starfish), A0A7E6FF05 (octopus), A0A2A3E996 (bee), T1FWN6 (leech), A0A5K4EUM0 (blood fluke), T2MBA6 (hydra), Q95YF0 (roundworm), A0A1X7V8T9 (sponge), Q8RWY6 (mouse-ear cress), A0A2K1K7V5 (moss), C1MNP8 (green alga), and P38198 (yeast). The tree was generated based on aligned amino acid sequences using the neighbor-joining method in the MEGA7 software.

Extended Data Table 1. X-ray data collection and refinement statistics.

Data collection	TOG4/CLIP170_CC Se (PDB id: 8WHH)	TOG4/CLIP170_CC native (PDB id: 8WHI)	TOG4/LL5β_TBM fusion (PDB id: 8WHJ)
Space group	$P\,2_12_12_1$	$P\,2_12_12_1$	$P\,4_1$
Cell dimensions			
a, *b*, *c* (Å)	86.115, 100.826, 226.065	52.624, 85.545, 114.195	51.132, 51.132, 97.935
α, β, γ (°)	90, 90, 90	90, 90, 90	90, 90, 90
Resolution (Å)	50–3.8 (3.87-3.8)	50–1.85 (1.88-1.85)	50–1.4 (1.42-1.4)
R_{merge}[a]	0.128 (1.212)	0.107 (1.686)	0.064 (0.822)
$I/\sigma I$	14.6 (1.3)	18.1 (1.2)	41.9 (2.9)
$CC_{1/2}$[b]	0.994 (0.838)	0.997 (0.576)	1.003 (0.890)
Completeness (%)	100 (100)	99.9 (100)	99.8 (99.8)
Redundancy	7.8 (8.0)	7.0 (6.8)	11.7 (9.7)
Refinement			
Resolution (Å)	50–3.8 (3.9-3.8)	50–1.85 (1.9-1.85)	50–1.4 (1.44-1.4)
No. reflections	37252 (2882)	44369 (2974)	49212 (3444)
R_{work} / R_{free}[c]	0.217 (0.315) / 0.266 (0.342)	0.191 (0.3) / 0.237 (0.382)	0.129 (0.165) / 0.174 (0.247)
No. atoms			
Protein	10075	3511	1998
Ligand/ion	0	19	8
Water	0	260	300
Mean *B* (Å)			
Protein	175	44.8	20.4
Ligand/ion	-	64.6	38.3
Water	-	46.6	33.6
r.m.s. deviations			
Bond lengths (Å)	0.004	0.01	0.008
Bond angles (°)	0.82	1.1	1.2
Ramachandran analysis			
Favored region (%)	99.84	99.31	99.6
Allowed region (%)	0.16	0.69	0.4
Outliers (%)	0	0	0

Continued on next page.

Data collection	TOG4/LL5β_CC (PDB id: 8WHK)	TOG4/CENP-E_CC (PDB id: 8WHL)	LL5β_EBM/ELKS2_CC3 (PDB id: 8WHM)
Space group	$P\,22_12_1$	$P\,6_1$	$C\,222_1$
Cell dimensions			
a, *b*, *c* (Å)	44.434, 69.294, 134.451	106.221, 106.221, 327.051	57.743, 90.716, 59.063
α, β, γ (°)	90, 90, 90	90, 90, 120	90, 90, 90
Resolution (Å)	50–2.4 (2.44-2.4)	50–3.2 (3.26-3.2)	50–2.3 (2.38-2.3)
R_{merge}[a]	0.065 (1.099)	0.080 (0.847)	0.164 (0.415)
$I/\sigma I$	35.8 (2.3)	14.8 (2.0)	9.1 (3.5)
$CC_{1/2}$[b]	0.999 (0.821)	0.991 (0.545)	0.995 (0.834)
Completeness (%)	99.8 (98.7)	99.9 (99.9)	99.2 (99.0)
Redundancy	11.2 (10.0)	6.3 (6.3)	4.6 (5.8)
Refinement			
Resolution (Å)	50–2.4 (2.55-2.4)	50–3.2 (3.29-3.2)	50–2.3 (2.9-2.3)
No. reflections	16702 (2620)	34200 (2847)	7108 (3503)
R_{work} / R_{free}[c]	0.206 (0.285) / 0.243 (0.344)	0.246 (0.315) / 0.278 (0.333)	0.257 (0.302) / 0.282 (0.326)
No. atoms			
Protein	2210	8740	1058
Ligand/ion	1	15	0
Water	33	0	21
Mean *B* (Å)			
Protein	79.3	121	41.1
Ligand/ion	59.1	112	-
Water	67.3	-	30.6
r.m.s. deviations			
Bond lengths (Å)	0.002	0.002	0.001
Bond angles (°)	0.62	0.48	0.29
Ramachandran analysis			
Favored region (%)	99.26	99.36	100
Allowed region (%)	0.74	0.64	0
Outliers (%)	0	0	0

The numbers in parentheses represent values for the highest resolution shell.

[a]$R_{merge} = \sum|I_i - I_m|/\sum I_i$, where Ii is the intensity of the measured reflection and I_m is the mean intensity of all symmetry related reflections.

[b]$CC_{1/2}$ is the correlation coefficient of the half datasets.

[c]$R_{work} = \Sigma||F_{obs}| - |F_{calc}||/\Sigma|F_{obs}|$, where F_{obs} and F_{calc} are observed and calculated structure factors.

$R_{free} = \Sigma_T||F_{obs}| - |F_{calc}||/\Sigma_T|F_{obs}|$, where T is a test data set of about 4-5% of the total reflections randomly chosen and set aside prior to refinement.

1218

Extended Data Movie 1. Live cell imaging of protein condensates in HeLa cells co-transfected with indicated constructs.

One image was taken every 20 seconds for 20 minutes. All scale bars are 1 μm.

Extended Data Movie 2. Live cell imaging of dynamic distribution of ELKS1 condensates and accumulated CLASP2α in the leading edge of a HeLa cell.

ELKS1 condensates with accumulated CLASP2α that remained visible during the recording are highlighted with white circles, while ELKS1 condensates that intermittently appeared and disappeared alone with the advancing leading edge were indicated by blue circles. One image was taken every minute for 2.5 hours. The scale bar is 10 μm.

Extended Data Movie 3. Live cell imaging showing the MT plus end moving across multiple ELKS1 condensates.

The MT plus end was indicated by CLIP170. One image was taken every 2 seconds for 1.5 minutes. The scale bar is 10 μm.

Extended Data Movie 4. Live cell imaging showing the disrupted condensate attachment by the 8S/D or +8D mutations in CLASP2α.

One image was taken every 20 seconds for 20 minutes. All scale bars are 1 μm.

Supplementary Files

This is a list of supplementary files associated with this preprint. Click to download.

- MovieS1copy.mp4
- MovieS2.mp4
- MovieS3.mp4
- MovieS4.mp4